6. Role of Secondary Fractures for Solute Transport in en Échelon Fault Zones

Abstract

Solute transport in hierarchical fracture networks associated with en échelon structures is investigated using a numerical model for network flow and advective-diffusive transport. Results are presented for cases that account for diffusion into both stagnant branch fractures and macroscopically unfractured matrix. Cases that are analyzed include both a deterministic geometry taken directly from a detailed fracture map from a site in southern Sweden, and a synthetic geometry based on statistics of maps.

For both cases, diffusion into stagnant branches increases retardation of solute, relative to simple advective-diffusive transport through the main en échelon segments in the absence of matrix diffusion. The retardation is less than for an equivalent two-domain model with equilibrium mass transfer between flowing and stagnant domains. Branch fractures thus may act as an additional type of immobile domain, beyond other hypothesized types of domains such as stagnant pools in channelized fractures or stagnant zones in gouge.

In cases with uniform fracture properties, stagnant branches increase the retardation of solute due to matrix diffusion, and the degree of late-time tailing. However, matrix diffusion is the dominant effect in terms of median arrival times for solute mass, for conditions representative of a repository in granitic rock. When fracture properties are heterogeneous, branch fractures can in some cases yield slightly lower net retardation when combined with matrix diffusion. This surprising result is interpreted as due to the interaction of flow-field heterogeneity and through-diffusion across fracture blocks. Where through-diffusion occurs, in some instances branch fractures may act as relatively rapid paths for solute to return to the flowing fractures.

From a practical standpoint in the context of a radioactive-waste repository, these results suggest that secondary fractures in en échelon structures are of net benefit in terms of radionuclide retention, but not sufficiently so to mitigate the otherwise poor retention characteristics of these structures. The effect of branch fractures on tailing of breakthrough curves may be important to recognize in analysis of in-situ tracer experiments, to avoid incorrect assessment of parameters for matrix diffusion models that will be applied over longer time scales.

6.1 Introduction

Groundwater flow in granitic rock is typically restricted to discrete fractures and fault zones. The flow and transport properties of these features are of concern, given proposals in several countries to build high-level radioactive-waste repositories in granitic rock (McCombie, 1997).

A generally understood principle of repository design in granitic rock is to avoid the fault zones on the larger scales likely to be encountered at a site (1 km to 10 km), which are likely to carry relatively high flows and to pose engineering difficulties for the underground construction process. The largest such zones are usually detectable by geophysical methods and borehole investigations, and hence they can usually be accounted for in the design process. However, blocks between such zones are commonly found to contain lesser-order fault zones, which are more difficult to detect prior to underground investigations, and which may therefore need to be accounted for in repository designs.

In this paper we consider the transport properties of a particular type of fault zone, which consists of discrete fractures arranged en échelon with linking fractures at stepovers. En échelon zones are of interest as one of the main types of hydraulically transmissive features that might be expected in a rock volume considered for a repository.

Field investigations (Martel *et al.*, 1988) indicate that en échelon zones represent an early stage of fault zone development, for low degrees of regional strain. Such a situation may be expected for rock volumes which are bounded by larger-scale fault zones that accommodate the major portion of regional strain. Thus en échelon zones are expected in volumes of sparsely fractured rock with a low degree of brittle deformation, which are sought as repository locations.

Field investigations at granitic sites in Sweden, including the present study, confirm that en échelon zones are found in rock volumes bounded by fault zones with more extensive brittle deformation, and that these en échelon zones can be traced over distances of up to tens of meters. Some of these zones are aligned nearly normal to the minimum principal compressive stress, and are hence likely to be transmissive in the present time.

En échelon zones may also have a relatively low potential for retardation of radionuclides leaking from a repository, in comparison with more extensively sheared fault zones. Matrix diffusion is the most significant mechanism for retention of radionuclides

leaking from a repository in granitic rock (Jakob, 2004), and is controlled by the interfacial area. In comparison with zones of more extensive brittle deformation, en échelon zones have relatively small interfacial area for matrix diffusion over most of their length (*i.e.* within the discrete en échelon segments).

However, detailed mapping of en échelon zones (Chapter 4) reveals a large number of small secondary fractures branching from the main en échelon segments, as well as intense fracturing within stepover zones. This is also predicted by theoretical models of compressive shear fault development (*e.g.*, Schulson *et al.*, 1999). These secondary fractures provide additional interfacial area via which diffusion into the matrix can take place. In this paper we explore the quantitative significance of secondary fractures for increasing the degree of radionuclide retardation along en échelon zones.

6.2. Method

To evaluate the potential effects of secondary fractures on solute transport through en échelon zones, we simulate flow and transport through deterministic and statistical, two-dimensional models. Steady-state flow through the models is computed by the finite-element method. Solute transport, including diffusion into stagnant branches and/or the rock matrix, is modeled by an advective-diffusive particle tracking algorithm described below. Comparison of cases with and without diffusion into stagnant secondary fractures, and cases with and without matrix diffusion, are used to evaluate the relative significance of these phenomena, as well as their combined effects.

Deterministic and statistical models of en échelon zones

The deterministic and statistical models are both based on detailed mapping of en échelon structures in granitic sites. The deterministic 2-D models are produced directly from a detailed map of an en échelon zone at the Äspö site in SE Sweden, as described by Geier *et al.* (2004). The statistical models were based on statistics from the Äspö site maps.

The deterministic model based on the Äspö map reproduces a 15 m long portion of a N-striking en échelon zone, in horizontal section. The map is adapted for numerical simulations (to simplify calculations of matrix diffusion) by conversion to a network of rectilinear segments (Figure 6-1). The model thus obtained has the advantage of not being filtered by any particular statistical model, and preserving details of architecture which may be overlooked in formulating a conceptual model for such zones.

The deterministic model has two main drawbacks for understanding the large-scale behavior of single en échelon zones. First it spans scales of only 15 m, and includes only a few stepovers, so does not represent averaging effects over longer transport distances involving multiple stepovers. Second, interpretation of the model results is complicated by the particular features such as the intersection with an ENE-striking feature of comparable order (between y = 5 m and y = 6 m in Figure 6-1). A model that represents a single en échelon zone in isolation, and at a higher level of abstraction, may be helpful for clarification of the main effects.

A statistical model was therefore constructed by statistical simulation of a 40 m long en échelon zone based on analysis of branching and stepover statistics from the Äspö site, including observations from the zone mapped in detail as well as similar structures in the vicinity. Key components of the model which are described in terms of probability distributions include: length of en échelon segments, the length of the stepovers, block size distribution within stepovers, and frequency and length of branch fractures of different orders (using the definition of branch order given in Section 3.2).

Outcrop mapping does not yield data on hydrologic properties (transmissivity or effective transport aperture). While apertures could be observed in a few of the fractures, here we take the view that apertures measured under stress-relieved and weathered conditions on bedrock outcrops are not a reliable indicator of apertures at depth. Instead, representative transmissivity values are chosen based on previous analyses of borehole data from Äspö (Geier *et al.*, 1995; Geier and Thomas 1996).

Uniform transmissivities are used for a given order of fractures. Field evidence suggests that the most realistic model would be one that includes variability of transmissivity both between and within individual fractures. However, variable-transmissivity models add additional degrees of complexity and uncertainty in the parameters, apart from the geometric properties which are the main focus of this study. Therefore we use a simplified representation of transmissivity in these models, recognizing that this is an idealization the implications of which could be explored through further analysis.

Effective apertures for transport are also assigned based on uniform, representative values for a given class of fractures. As with transmissivity, effective transport aperture are likely to be variable. The nature of this variation under in situ conditions is poorly known, due to the difficulty of performing in situ transport experiments with unequivocal interpretations. For the present study, representative values were chosen based on results of past investigations of single-fracture transport properties in similar geologic settings, as reviewed in Chapter 2.

The statistical distributions used to generate the network models are summarized in Table 6-1. Examples of stochastic realizations are shown in Figure 6-2, which may be compared with the actual outcrop map in Figure 6-1.

The simulated en échelon zone in Figure 6-2 is an abstraction in several respects. A rectilinear configuration of segments is used to simplify the problem of computing fracture

intersections, and to reduce the chance of the numerical difficulties in the flow and solute transport computations due to an ill-conditioned finite-element mesh. The complex architecture of fracturing within the stepovers between en échelon segments is idealized as a simple, hierarchical fragmentation process. Intersecting fracture zones such as those seen on the outcrop are excluded, to focus on the transport properties of a single en échelon zone.

Despite these idealizations, the models reproduce approximately the geometric properties observed on the outcrop that were anticipated to be key for transport, as discussed in the foregoing paper. These aspects are (1) the length distribution of the main en échelon segments, (2) the frequency of branching secondary fractures (such as splays or pinnate fractures) of various orders, (3) the length distributions for different orders of branches, and (4) the block size distribution and fracture intensity within the stepovers between en échelon segments.

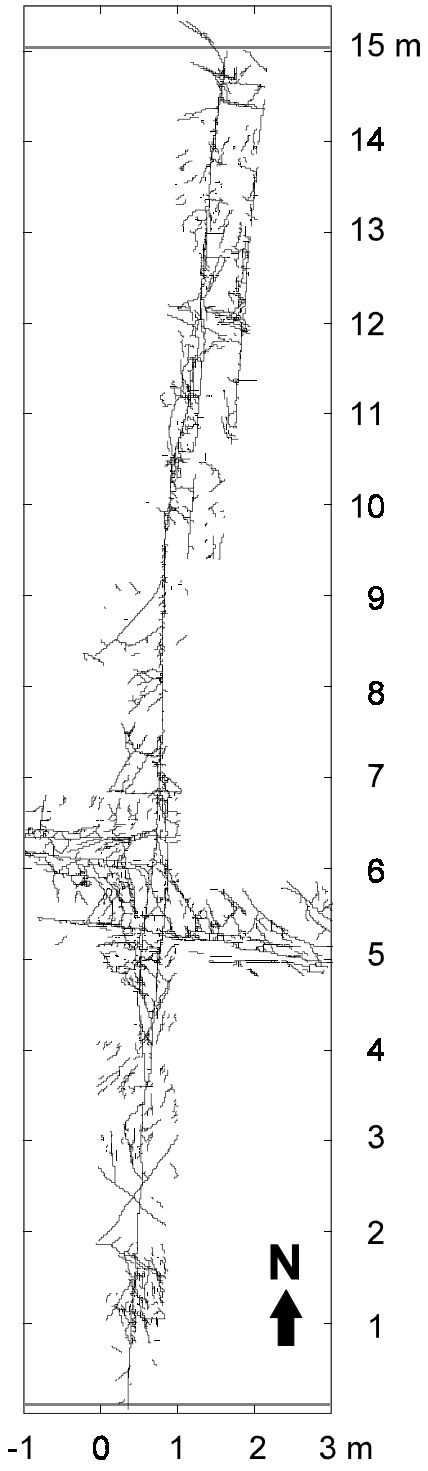

Figure 6-1 Rectilinear network model for flow and transport simulations, based on detailed en échelon zone map from Äspö site, using a discretization level of 2 cm.

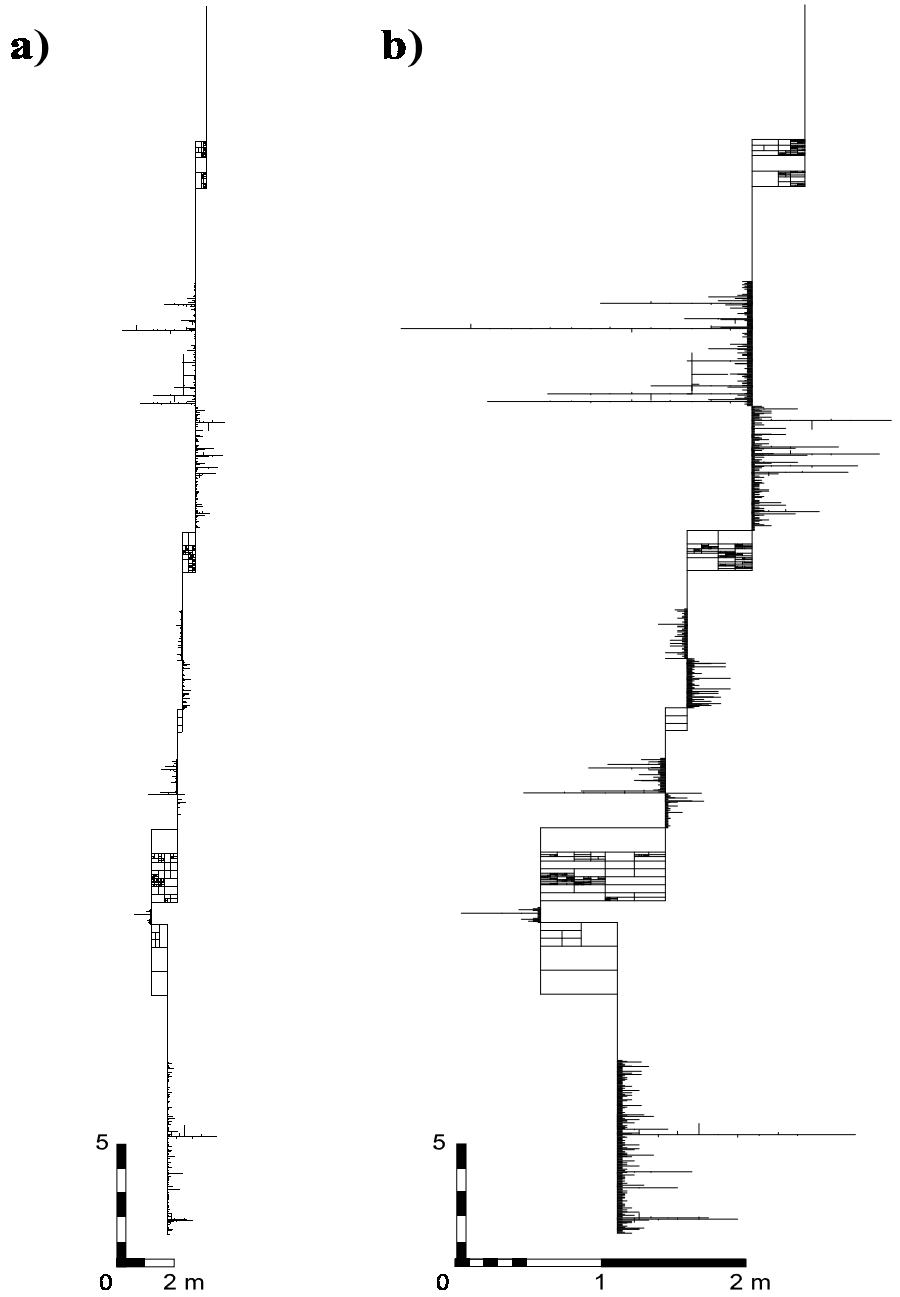

Figure 6-2. A single realization of a 40 m long section of en échelon zone simulated based on a rectilinear statistical model (revised version)for stepovers and branch fractures in en échelon zones on Äspö, shown (a) with equal scales in horizontal (E-W) and vertical (N-S) directions, and (b) with horizontal (E-W) scale exaggerated by a factor of 5 to show frequency of small wing/pinnate fractures.

Table 6-1: Parameters and statistical models for en échelon fracture zones

1. Deterministic model:		
Segment transmissivity T_{seg}	$1x10^{-7}$ m^2/s	
Segment transport aperture b_{seg}	0.5 mm	
2. Stochastic geometric model		
Length of en échelon segments L_0:	U[5 m, 15 m]	
Length of en échelon segment overlaps (stepovers):	U[0.5m, 2.5 m]	
Aspect ratio of stepovers:	U[3,5]	
Sense of step-overs:	P[right-stepping] = 0.8;	
	P[left-stepping] = 0.2	
Branch fracture frequency f_i (I = order of branch):	f_1	36.3 per m
	f_2	7.53 per m
	f_3	2.42 per m
Branch length distribution L_i (I = order of branch):	L_1	P_L(2.75,0.02 m)
	L_2	P_L(2.55,0.02 m)
	L_3	P_L(2.75,0.02 m)
Stepover fragmentation fractal dimension	D_f = 1.5	
Transmissivity (heterogeneous case)	T_0	$1x10^{-7}$ m^2/s
(T_i, I = order of branch)	T_1	$2x10^{-8}$ m^2/s
	T_2	$1x10^{-8}$ m^2/s
	T_3	$1x10^{-9}$ m^2/s
Transmissivity (uniform case)	T_i	$1x10^{-7}$ m^2/s
Transport aperture (heterogeneous case)	b_0	0.5 mm
	b_1	0.2 mm
	b_2	0.1 mm
	b_3	0.05 mm
Transport aperture (uniform case)	b_i	0.5 mm

$U[x_{min}, x_{max}]$ = uniform distribution of the parameter x in the range $x_{min} \leq x \leq x_{max}$

$P_L[D, x_{min}]$ = power-law distribution of the parameter x with exponent D and minimum value x_{min}.

Simulation of groundwater flow

Steady-state flow of groundwater through the en échelon-zone models is calculated using the *dfm* finite-element code as described by Geier (2004). The steady-state flow is a function of the fracture transmissivities and the imposed head gradient between the end points along strike.

Values of transmissivity are assigned choosing representative values of single-fracture transmissivity based on past analyses of hydraulic test data at Äspö (Geier *et al.* 1995; Geier and Thomas 1996). For the deterministic case, the same uniform value was assigned to all fracture segments. For the synthetic model, two separate cases were used, one with uniform hydraulic properties and the other with heterogeneous properties (values depending on the order of branch fractures in the model).

A hydraulic gradient of 0.025 was imposed by assigning a head differential of 0.375 m across the 15-m length of the Äspö map. A 1 m head differential was applied to the 40 m long synthetic model, to give the same hydraulic gradient for all cases. A hydraulic gradient of 0.025 is at the high end of the range of gradients that can reasonably be expected for a repository in granitic rock in Sweden (Dverstorp *et al.*, 1996).

Gradients of this magnitude are of practical concern for a high-level radioactive-waste repository in granitic rock. In low-relief regions of granitic bedrock such as southern Sweden, head differentials on the order of 1 m over a 40 m scale are most likely to occur in relatively "good" rock which has low fracture intensity and low effective hydraulic conductivity. Current repository siting concepts for granitic rocks favor locating radioactive wastes in such blocks (*e.g.*, SKB, 1999). In such a block, an en échelon zone consisting of a small number of favorably connected fractures could act as a discrete flow path through an otherwise low-conductivity block of rock.

The variation of hydraulic head and groundwater flow rates in the deterministic network and in the synthetic network model are illustrated in Figures 6-3 and 6-4, respectively. The synthetic zone carries a groundwater flow per 1 m thickness (in the vertical direction) of 5.3×10^{-10} m^3/s (1.92 ml/hr or 16.8 liters per year). The corresponding advective velocity in the main en échelon segments, for an assumed mean aperture of 0.2 mm, is 2.7×10^{-6} m/s (9.6 mm/hr or 84 m/yr). The mean advective velocity along the entire zone, based on the median water-residence time determined by advective-diffusive particle tracking, is 1.95×10^{-6}

m/s (7.0 mm/hr or 61 m/yr). The mean velocity is lower than the velocity within the main en échelon segments, due to slower passage through the stepover zones, where the high fracture intensity implies larger pore volumes per unit distance along strike.

The mean velocity of 61 m/yr is on the high end of what is typically considered a reasonable range for repository conditions, but probably on the low end for in-situ tracer tests.

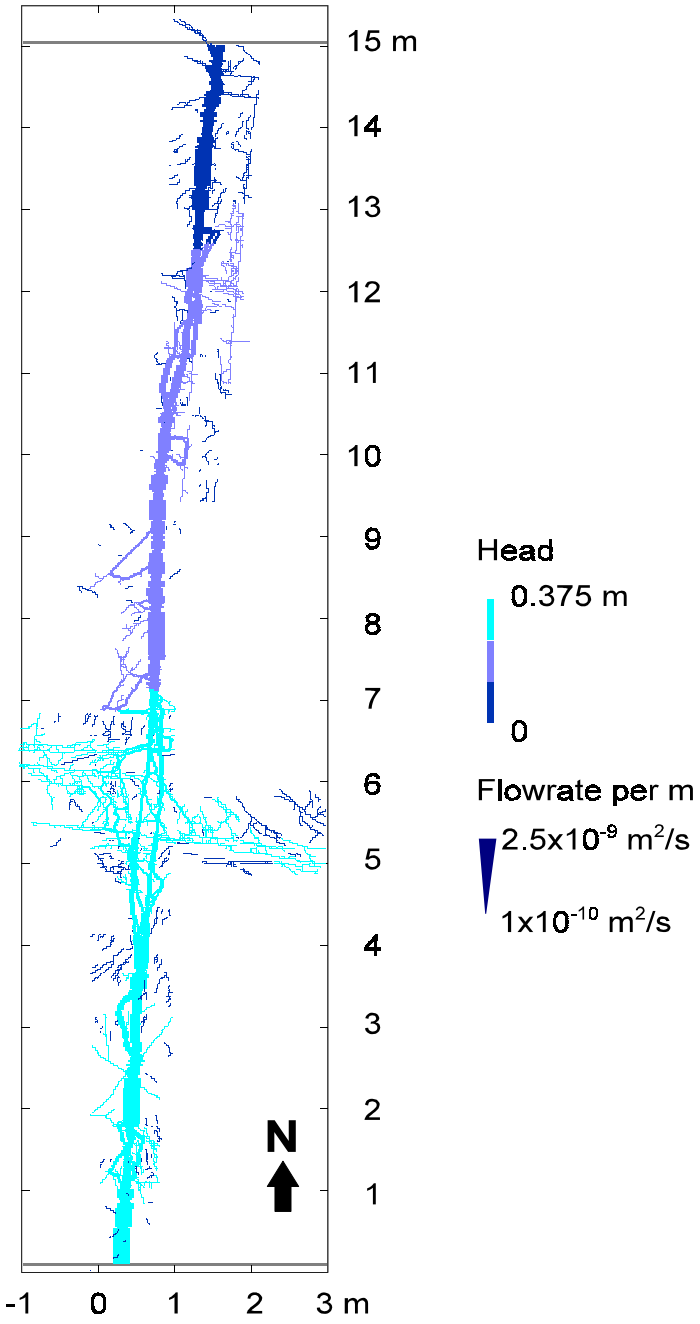

Figure 6-3. Head and flow field calculated for 2-D fracture network defined by Äspö en échelon zone map, for 1 m gradient applied south to north. Head in fractures is indicated by color scale. Flow rate is proportional to line width (except for stagnant fractures which are represented by the narrowest lines). A digital version of this plot which can be viewed at higher resolution is provided in the electronic supplement.

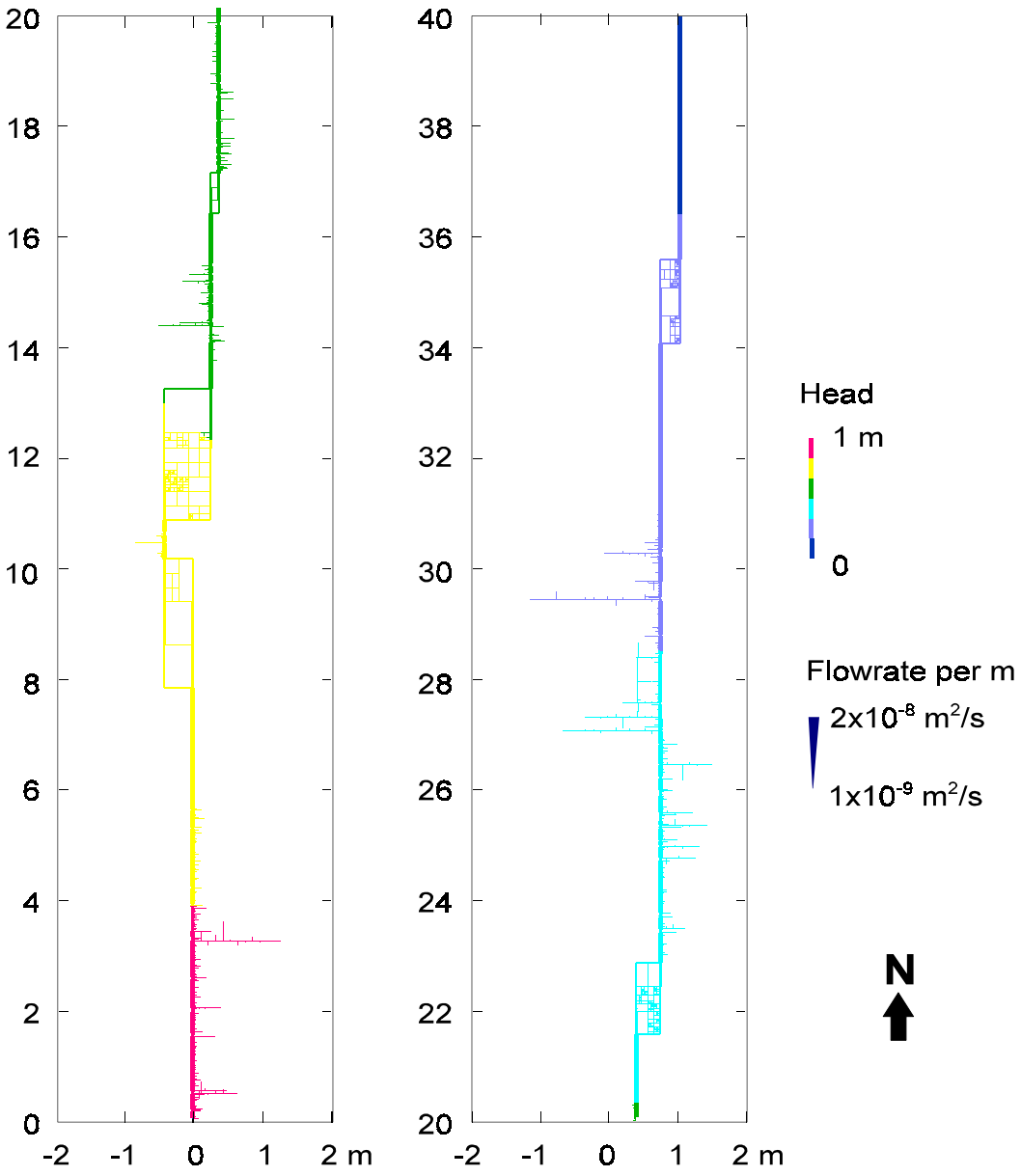

Figure 6-4. Head and flow field calculated for 2-D synthetic en échelon zone, for 1 m gradient applied south to north. Head in fractures is indicated by color scale. Flow rate is proportional to line width (except for stagnant fractures which are represented by the narrowest lines). Note the plot has been split into two sections to allow plotting at a larger scale on the page. A digital version of this plot which can be viewed at higher resolution is provided in the electronic supplement.

Simulation of advective-diffusive transport in fracture segments

Transport of solute through the fracture network and in the adjoining rock (matrix) is simulated by an advective-diffusive particle-tracking method. The method for tracking particles through fracture intersections is inspired by the conceptualization of Park *et al.* (1999), but the algorithm used here permits diffusion into stagnant branches. The following is a brief summary; full details of the method are given in Chapter 3.

Within a given 1-D fracture segment, advective-dispersive transport is modeled by a discrete-parcel random walk algorithm (Ahlstrom *et al.*, 1977), following the suggestion of Detwiler *et al.* (2000) and Bruderer and Bernabé (2001) to account for Taylor dispersion resulting from diffusion in combination with velocity variations across the aperture, by tracking particles in this dimension (here denoted *z*).

Each discrete parcel or "particle" represents a fixed mass m_p of solute, which moves through the network and/or matrix as a random walk. A particle's displacement during a single step of the random walk, representing a small time interval Δt, is the sum of a random, diffusive component $(\Delta x_d, \Delta z_d)$ and an advective component Δx_a which is equal to Δt times the average velocity over the diffusive trajectory during the time interval, taking into account possible "bounces" off the fracture wall as described below.

If the Δz_d component is large enough to cause the particle to move beyond the boundaries of the fracture segment (*i.e.* the fracture walls), the particle may either enter the adjoining matrix with probability P_m, or else "bounce" off the fracture wall with reflected motion. The local velocity $v(z)$ at a given height z above the median surface within a given fracture segment is assumed to follow the parabolic velocity profile for Poiseuille flow with no-slip conditions at the fracture walls:

$$v(z) = \frac{Q}{b}\left[\frac{3}{2} - \frac{6z^2}{b^2}\right] \tag{6-1}$$

where Q is the flow through the fracture segment per unit thickness (obtained from the finite-element solution) and b is the local value of fracture aperture.

Routing and mixing of solute at junctions between fracture segments

Routing of solute at junctions between fracture segments is modeled by an explicit algorithm for diffusion across streamlines within the junctions, with the simplifying assumption of an idealized junction geometry as suggested by Park and Lee (1999).

Models of solute transport in fracture networks have commonly been based on either of two end-member assumptions for routing of solute at intersections: streamline routing with no mixing across streamlines or complete mixing. Detailed modeling of flow and transport through fracture intersections (Berkowitz *et al.*, 1994; Park *et al.*, 2001) has shown that the degree of mixing is related to the Peclet number $Pe = av/D_m$ where v is the fluid velocity and a is a characteristic length for the intersection. For high Pe the rate of diffusion across streamlines is small relative to the advective velocity, and streamline routing may be a better approximation. For low Pe the rate of diffusive transport across streamlines is large relative to the rate of advection, and complete mixing may be a good approximation. At intermediate values of Pe, intermediate forms of routing may occur. Thus for a fixed geometry, the degree of mixing for flow through the intersection varies with the fluid velocity.

We consider partitioning of solute at junctions with three, four, or more branches. For brevity, we use the notation J_i to denote the class of junctions with I branches, so a J_3 junction has three branches, a J_4 junction has four branches, *etc*.

If one fracture terminates at its intersection against another fracture (a common case in natural fracture networks as pointed out by Dershowitz 1984), the junction is of type J_3. The distinction between streamline-routing and complete-mixing rules is irrelevant for a J_3 junction, if all three branches are non-stagnant and if the branches are longer than mixing length L_{mixing} at which fully mixing across the aperture can be assumed. Either the solute flux from one well-mixed inlet branch is divided according to the flow ratio between two outlet branches, or the solute fluxes from two inlet branches are combined in one outlet branch, and become well-mixed at distance L_{mixing} along that branch. However, when one branch of a J_3 junction is stagnant, solute enters and exits that branch only by diffusion, and this process must be accounted for in the mixing rule for the junction.

A J_4 junction results whenever two fractures intersect each other and both fractures are through-going. Junctions of higher order (J_5, J_6, *etc*.) require a larger number of fractures to share a common intersection, but are occasionally found in nature as well as in synthetic,

stochastically generated fracture networks.

When all branches of a J_4 or higher-order junction are non-stagnant, the entry and exit points of streamlines from a junction can be defined by considering the branches in cyclic order (either clockwise or counterclockwise). Topological constraints in a two-dimensional network model, where flow is driven by potential gradients, ensure that all branches of a junction with positive inflow lie to one side of all branches with positive outflow, when the branches are placed thus in cyclic order (Bruderer and Bernabé, 2001). Finding the inlet and outlet streamline locations is then straightforward: starting from a neighboring pair of inlet and outlet branches, the streamlines must pass through points that bound an equal fraction of the inflow and outflow.

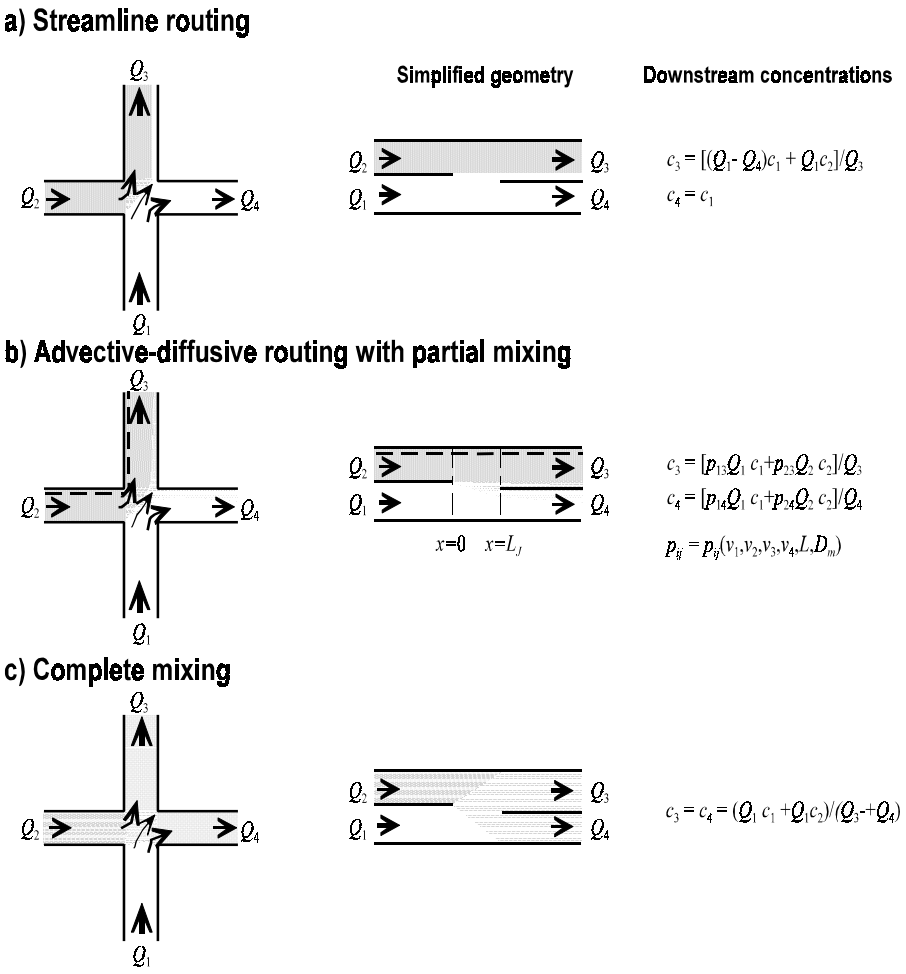

Figure 6-5. Alternative rules for routing of solute at four-branch junctions in a 2-D fracture network.

The position of the streamlines within the intersection are needed in order to model solute transfer due to diffusion across streamlines within the junctions. In detailed studies of individual junctions this problem has been addressed by numerical solution of the Navier-Stokes equation (Berkowitz *et al.*, 1994) or lattice-gas simulation (Stockman *et al.* 1997), but such detailed sub-models are not practical for the network-scale problems we address here.

Park and Lee (1999) proposed modeling advective-diffusive transport through junctions based on a simplified, "folded-up" geometry, as depicted in the right-hand side of Figure 6-4. Park and Lee gave analytical solutions for the probabilities p_{ij} for a particle to pass from inlet branch I to outlet branch j, as functions of the inlet/outlet flow rates and velocities J_4. These solutions are singular for the case of stagnant branches, so not applicable for the general case we consider, but they are useful for verifying the particle-tracking algorithm for non-stagnant cases.

Here we follow the conceptual approach of Park & Lee (1999) by modeling transport through an idealized junction of simplified geometry, but in place of their analytical solutions we use explicit advective-diffusive particle-tracking through the simplified junctions, in order to address the additional complication of diffusion into and out of stagnant branches.

Representation of stagnant branches

We represent the interface between a stagnant branch and a junction as an interface of infinitesimal thickness, with position depending on the cyclic position of the stagnant branch relative to the flowing branches (Figure 6-6a through 6-6d). In a real junction, the mouth of each stagnant branch is a zone of interaction with flowing water. Diffusive transfer takes place across some curved surface which spans the aperture of the stagnant branch. For a viscous fluid and laminar-regime flow, in reality this is a gradational rather than distinct interface. As a key approximation in our idealized model for junctions with stagnant branches, we idealize this zone of interaction as an abrupt interface, with length equal to the aperture of the stagnant branch.

If the trajectory of a solute particle undergoing advective-diffusive motion in the flowing part of the junction happens to intersect this interface, the particle enters the corresponding stagnant branch with residual motion equal to the residual component of transverse diffusion.

Within the stagnant branch, the particle is postulated to move by purely diffusive motion as described above until it either interacts with the matrix or returns to the mouth of the stagnant branch. In the latter case, the particle will re-enter the flowing portion of the junction, via the same interface but in the reverse direction. The coordinates of the particle as it re-enters the junction are obtained by mapping its position within the stagnant-branch aperture onto the corresponding position on the interface representing the branch in the idealized junction.

Simulation of diffusive transport in the matrix

An explicit particle-tracking algorithm is used to represent diffusion in the matrix. More efficient methods of simulating matrix diffusion with particle-trackers have been presented, for example, by Dershowitz and Miller (1995), Delay and Bodin (2001), and Tsang and Tsang (2001). All of these make use of idealizations regarding the geometry and extent of the matrix volume into which solute diffuses, and assume that solute eventually returns to the same fracture from which it enters the matrix. Delay and Bodin (2001) also note that their method is singular for the case of stagnant fluid in the fracture.

Here we use an computationally expensive but explicit method, which accounts for both the finite depth of matrix available for diffusion (depending on fragment size), and the possibility that solute may diffuse from one fracture to another. For the results presented here, over 10% of solute diffusing into the matrix from a given fracture was found to re-emerge in a different fracture. This indicates that transfer of mass by diffusion between fractures may be significant for the network geometries and time scales considered here.

The probability P_m of a particle entering the matrix pore space on a given collision with a fracture wall is assumed to be equal to the local matrix porosity θ_m. Matrix porosity is assumed to be uniform and isotropic. This idealization is adopted in order to focus on the role of en échelon zone and secondary fracture geometry, as the main topic of investigation for this study. Experimental data exist to support more heterogeneous models of matrix porosity (Xu *et al.*, 2001) which could be considered with minor modifications of the algorithm.

Transport for particles in the matrix is simulated in the same way as transport in the fracture, except that random diffusive motions are proportional to the square root of effective matrix diffusivity D_p, rather than of the molecular diffusion coefficient D_m. Advection in the

matrix is assumed to be negligible, so only the diffusive component of particle motion is modeled. In the type of rocks considered here, the hydraulic conductivity of macroscopically unfractured matrix is on the order of 10^{-13} m/s, and due to the well-connected nature of the en échelon fracture system, local hydraulic gradients are on the order of 1 or less. For a matrix porosity $\theta_m = 0.005$ as used here, this implies advective velocities through the matrix on the order of $2x10^{-11}$ m/s, as compared with advective velocities on the order of 10^{-6} m/s in the fractures.

At each time step for a particle in the matrix, a check is made of whether the particle motion intersects the wall of any fracture segment. If so the particle motion through the matrix is truncated at the fracture wall, and the particle moves into the fracture segment. This segment need not belong to the same fracture or fracture segment from which the particle initially entered the matrix.

Thus the method explicitly accounts for the variable, finite size of matrix blocks within the en échelon zone, and allows through-diffusion of particles from one fracture to another, even if the fractures are not directly connected. This contrasts with algorithms of Dershowitz and Miller (1995) and of Tsang & Tsang (2001) which treat diffusion as an effectively 1-D process out of and back into a single given fracture.

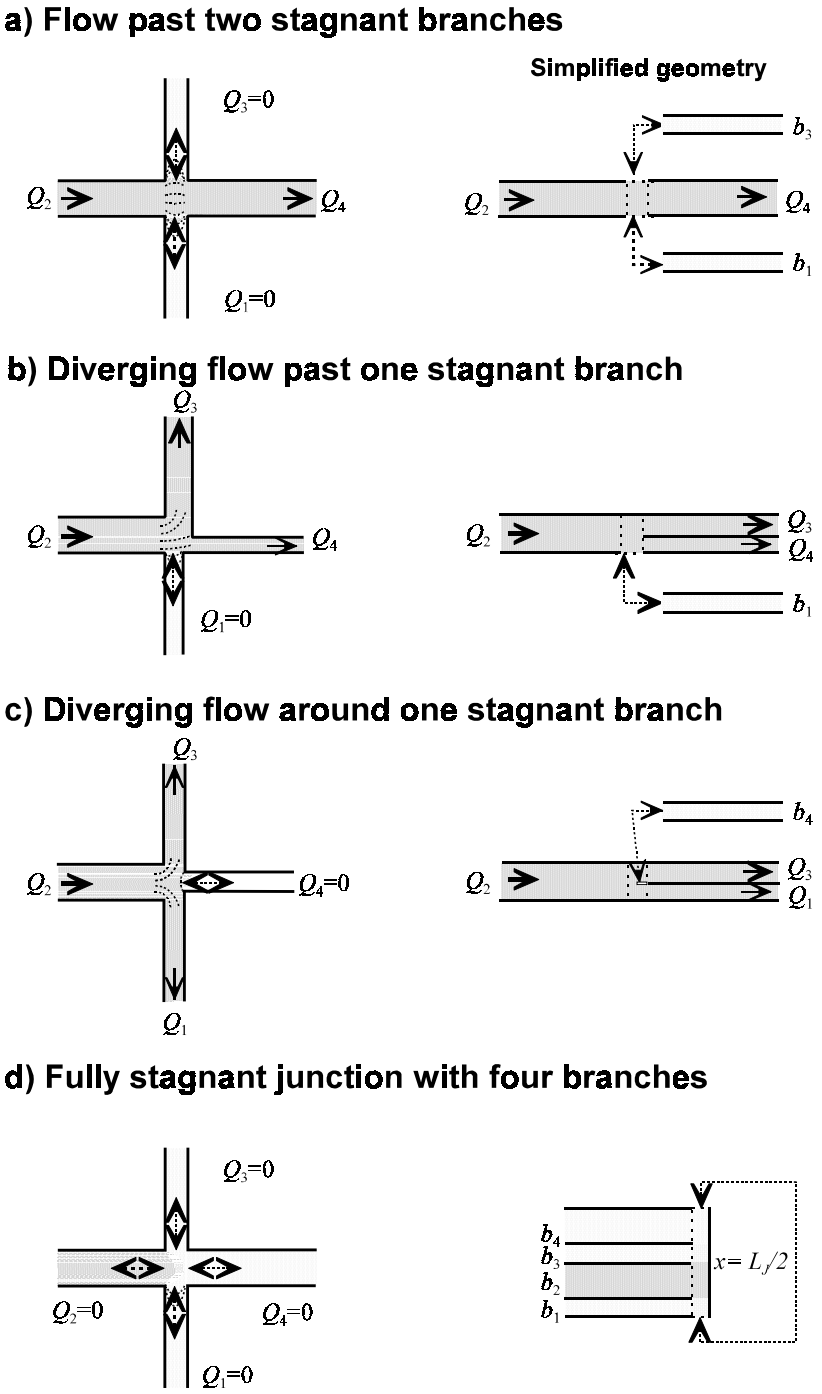

Figure 6-6. Examples of junctions with stagnant branches, and their simplified geometric representation.

Simulations of network-scale transport

For the present study, the algorithms described above have been implemented in a C language program, *meshtrak2d*, and verified with respect to a set of simple test networks for which the results could be predicted analytically. Further documentation of this program including source code and results of verification cases are provided as an electronic appendix by Geier (2004).

Simulations of the following cases were conducted to assess the relative effects of stagnant branches and matrix diffusion in terms of solute break-through:

Case AD: Advective-diffusive transport in the flowing fractures (the network backbone), with no diffusion into stagnant branches or into the matrix.

Case ADB: Advective-diffusive transport in flowing fractures and diffusion into stagnant branches, but no matrix diffusion.

Case ADM: Advective-diffusive transport in flowing fractures and matrix diffusion, but no diffusion into stagnant branches.

Case ADBM: Advective-diffusive transport in flowing fractures with diffusion into both stagnant branches and the matrix.

For the last two cases matrix properties were assumed to be uniform. Sorption was not included in any of the runs, nor was radioactive decay. For the cases with matrix diffusion, values of matrix diffusivity $D_p = 2\text{x}10^{-11}$ m^2/s and matrix porosity $\theta_m = 0.005$ were assumed based on recommended values for Swedish granitic rock from Ohlsson & Neretnieks (1995).

For each case, 1000 particles, each representing an arbitrary fixed mass of solute m_p, were released at the inflowing edge of the network (the southern end) at time t=0 and tracked until they emerged at the outflowing edge (the northern end). Thus the input was in the form of a Dirac delta pulse of mass $1000m_p$.

At each end, only one fracture (a main en échelon segment) intersected the boundary, so nearly all particles entered and left the simulated network via these fractures. For the cases that included matrix diffusion, a small number of particles (less than 1%) exited the 40 m long section while diffusing through matrix adjacent to the main en échelon segment, after entering the matrix a few millimeters from the upstream or downstream boundary.

6.3 Results and Analysis

Figure 6-7 through 6-9 show the solute breakthrough curves for the deterministic and synthetic cases, each comparing the four cases of simple advection-diffusion without and with diffusion into stagnant branches (Cases AD and AD+B, respectively), and the same cases including matrix diffusion (Cases AD+M and AD+B+M). The accompanying tables (Tables 6-2 through 6-4) give transport statistics in terms of the temporal moments at the outlet defined as (*e.g.*, Cunningham and Roberts, 1998):

$$m_n = \int_0^\infty t^n c_o(t)\,dt \tag{6-2}$$

where $c_o(t)$ is the concentration at the outlet as a function of time t, and in terms of the percentiles t_p representing the times at which p percent of the mass has arrived at the outlet, for a Dirac delta pulse release at the inlet.

Comparison of the first two cases (AD and AD+B) shows that the effect of branch fractures in retarding solute transport is less than would be expected from simple consideration of the ratios of stagnant to mobile water volumes along the en échelon zones. To quantify this effect, we define the retardation factor due to branch fractures as:

$$R_B = \frac{v_{AD}}{v_{AD+B}} = \frac{m_{1(AD+B)} / m_{0(AD+B)}}{m_{1(AD)} / m_{0(AD)}} \tag{6-3}$$

where v_{AD} is the mean nominal velocity of solute (transport distance divided by the mean transport time which is equal to m_1/m_0) in Case AD, and v_{AD+B} is the corresponding mean nominal velocity for Case AD+B.

If the branch fractures acted as stagnant volumes in equilibrium with the flowing water, we would expect the value of R_B to be simply the ratio of the total pore volume (flowing fractures and stagnant branches) to the flowing fracture volume. For the deterministic case, this ratio is 6.6 based on the values in Table 6-1. For the synthetic case, this ratio is 3.4.

The actual values of R_B obtained from the solute transport modeling are lower for the cases with uniform fracture hydraulic properties, with $R_B = 1.44$ in the deterministic case and $R_B = 2.2$ in the synthetic case. A higher retardation $R_B = 4.0$ is obtained for the heterogeneous case of the synthetic model.

In both homogeneous cases, the retardation in the models is less than the estimate from a simple calculation of the volume ratios. This is expected since a given first-order branch is guaranteed to be in equilibrium with the mobile water only at the end connecting from the fracture. Other portions of the branch (as well as higher-order branches) have a time-dependent response, so the actual R_B is only a fraction of the potential R_B as estimated from the volume ratios. The difference between actual and potential R_B can be expected to decrease with decreasing v_{AD}, as the time scale for advection along the flowing fractures approaches the time scale for diffusion into the branches.

Stagnant volumes connected to flowing areas of fractures have been invoked as an explanation for tracer residence times longer than expected based on aperture measurements, in in-situ experiments in granitic rock (Abelin *et al.*, 1985; Abelin *et al.*, 1990; Poteri *et al.*, 2002). Hypotheses have included stagnant "pools" within channelized fractures (Abelin *et al.*, 1990) as well as immobile water within gouge and breccias in complex fractures (Mazurek *et al.*, 2003; Poteri *et al.*, 2002). The results given here indicate possible significance of an additional type of immobile domain due to secondary (branch) fractures, supported by geometric evidence from detailed mapping. This additional type of immobile domain need not preclude other hypotheses that have been proposed, and indeed may well occur alongside of the other types of domains which have not been considered here.

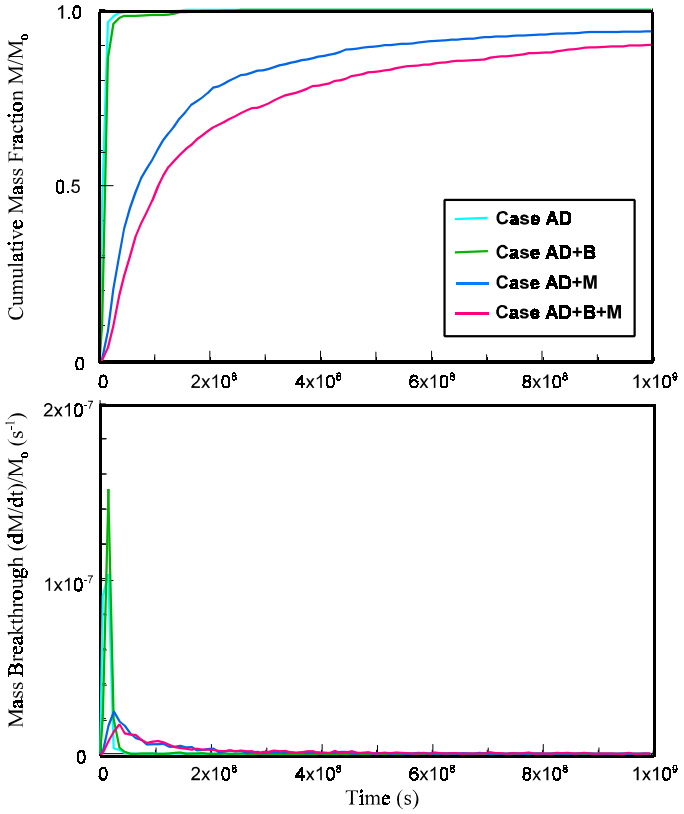

Figure 6-7 Solute breakthrough curves at north end of deterministic model with $D_p = 2x10^{-11}$ m^2/s, $\theta_m = 0.005$, $N_p = 1000$. Cases as defined in text.

Table 6-2. Moments and percentiles of solute breakthrough times for deterministic model. Statistics are given for $t' = t/(1x10^7$ s) where t is the breakthrough time for a given mass of solute. Moments M_1, M_2, and M_3 are normalized with respect to M_0, the total solute mass (equal to the number of particles N times the solute mass per particle, which is arbitrary).

Case	N	M_1/M_0	M_2/M_0	M_3/M_0	t'_{05}	t'_{10}	t'_{25}	t'_{50}	t'_{75}	t'_{90}	t'_{95}
AD	1000	1.19	2.19	0.122	0.80	0.83	0.90	1.03	1.23	1.56	1.79
AD+B	1000	1.71	6.03	62	0.93	1.00	1.15	1.38	1.75	2.2	2.7
AD+M	996	27	560	$2.4x10^6$	1.57	2.1	3.5	7.5	19	52	120
AD+BM	997	60	$2.1x10^5$	$2.0x10^9$	2.3	3.0	5.1	11.2	33	99	193

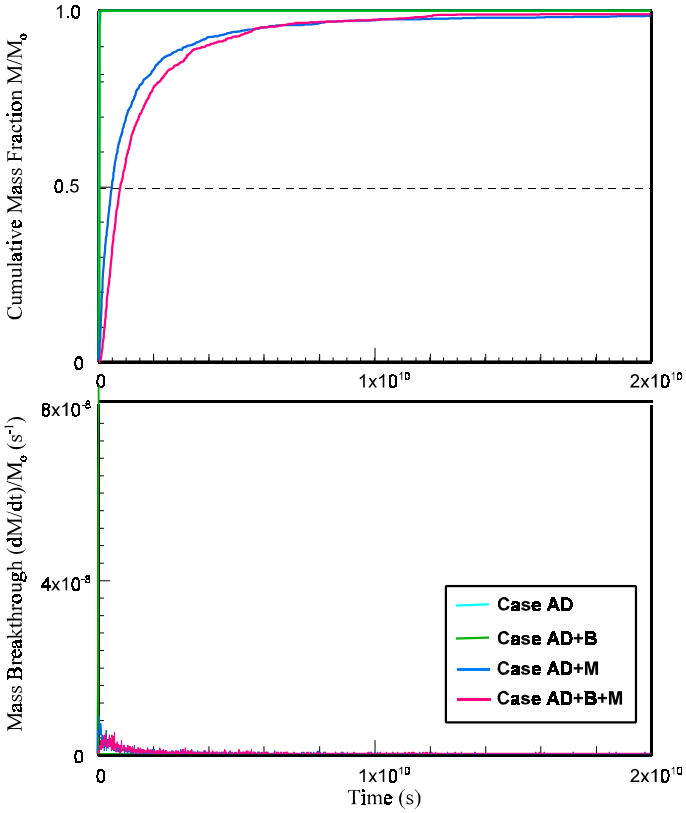

Figure 6-8 Solute breakthrough curves at north end of synthetic model (uniform hydraulic properties in all fracture segments) with $D_p = 2x10^{-11}$ m^2/s, $\theta_m = 0.005$, $N_p = 1000$.

Table 6-3. Moments and percentiles of solute breakthrough times for synthetic model (uniform hydraulic properties). Statistics are given for $t' = t/(1x10^7$ s) where t is the breakthrough time for a given mass of solute. Moments M_1, M_2, and M_3 are normalized with respect to M_0, the total solute mass as in Table 6-2.

Case	N	M_1/M_0	M_2/M_0	M_3/M_0	t'_{05}	t'_{10}	t'_{25}	t'_{50}	t'_{75}	t'_{90}	t'_{95}
AD	1000	1.67	2.9	5.5	1.45	1.49	1.56	1.64	1.74	1.84	1.90
AD+B	1000	3.7	13.9	55	2.5	2.7	3.1	3.6	4.1	4.6	4.9
AD+M	991	177	$3.5x10^5$	$1.70x10^9$	5.1	8.1	16.6	49	129	320	590
AD+BM	997	184	$1.79x10^5$	$5.13x10^8$	15.5	23	42	80	181	390	580

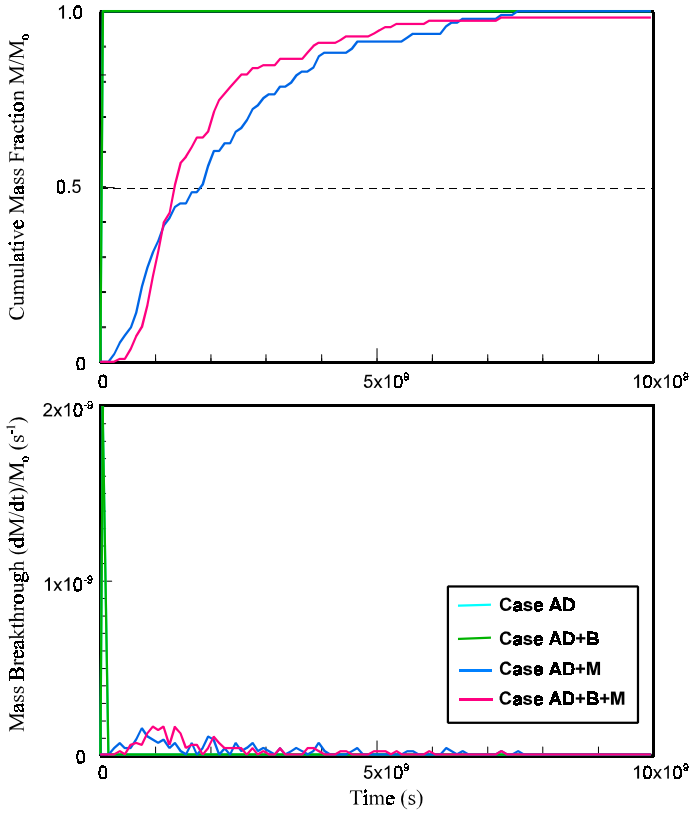

Figure 6-9 Solute breakthrough curves at north end of synthetic model (heterogeneous hydraulic properties) with $D_p = 2x10^{-11}$ m^2/s, $\theta_m = 0.005$, $N_p = 100$ (Cases AD+M and AD+B+M) to 1000 (Cases AD and AD+B).

Table 6-4. Moments and percentiles of solute breakthrough times for synthetic model (heterogeneous hydraulic properties). Statistics are given for $t' = t/(1x10^7$ s) where t is the breakthrough time for a given mass of solute. Moments M_1, M_2, and M_3 are normalized with respect to M_0, the total solute mass as in Tables 6-2 & 6-3.

Case	N	M_1/M_0	M_2/M_0	M_3/M_0	t'_{05}	t'_{10}	t'_{25}	t'_{50}	t'_{75}	t'_{90}	t'_{95}
AD	1000	2.3	5.4	13.4	2.1	2.1	2.1	2.2	2.3	2.5	2.7
AD+B	1000	9.2	86	830	7.0	7.4	8.1	9.0	10.0	11.0	11.6
AD+M	93	2200	$8.0x10^6$	$3.7x10^{10}$	360	600	870	1870	3000	4600	6200
AD+BM	111	1990	$6.7x10^6$	$3.7x10^{10}$	670	860	1030	1400	2300	3900	5100

Non-equilibration between branch fractures and the mobile fractures is also indicated by skewed breakthrough curves, with heavier late-time tails than the Gaussian curve expected for simple advection with Taylor dispersion through the flowing fractures. In terms of the random-walk model of diffusion processes, this may be understood as longer residence times for the fraction of particles that happen to enter stagnant fractures, with variable stagnant-fracture residence times related to the length of the stagnant branches and depth of the stagnant network.

Matrix diffusion either without or without stagnant branches (Cases AD+M and AD+B+M) produced a much larger retardation than stagnant branches alone. We define retardation factors for these two cases as:

$$R_M = \frac{v_{AD}}{v_{AD+M}} = \frac{m_{1(AD+M)} / m_{0(AD+M)}}{m_{1(AD)} / m_{0(AD)}} \tag{6-4}$$

$$R_{BM} = \frac{v_{AD}}{v_{AD+B+M}} = \frac{m_{1(AD+B+M)} / m_{0(AD+B+M)}}{m_{1(AD)} / m_{0(AD)}} \tag{6-5}$$

where v_{AD+M} and v_{AD+B+M} are the median nominal velocities of solute for Cases AD+M and AD+B+M respectively.

For the case of matrix diffusion from flowing fractures without stagnant branches (Case AD+M), the values of R_M are 23 and 106 for the deterministic and synthetic (uniform) cases, respectively, and R_M = 960 for the synthetic, heterogeneous case. Thus the retardation due to ordinary matrix diffusion, ignoring the branches, is much greater than that due to stagnant branches, for the representative values of head gradient, matrix porosity, and matrix diffusivity considered here. The breakthrough curves for these cases are also skewed.

When diffusion into stagnant branches is included along with matrix diffusion (Case AD+B+M), the values of R_{BM} are 50 and 110 for the deterministic and synthetic (uniform) cases, respectively, and R_{BM} = 865 for the synthetic, heterogeneous case. Thus in the deterministic case, the additional access to the matrix provided by the stagnant branches enhances the retardation due to matrix diffusion by roughly a factor of two. For the synthetic model, the relative significance of the branch fractures is lower, even in the case with uniform hydraulic properties.

The effects of stagnant branches and heterogeneity on retardation in the respective cases are illustrated by the plots of solute distribution in Figures 6-10 through 6-14. All of these plots represent cases in which matrix diffusion is included. In the pairs of synthetic-model figures representing the uniform case (6-11 & 6-12) and heterogeneous case (6-13 & 6-14), the second figure pair includes diffusion into stagnant branches. The synthetic model results are plotted for longer time scales to show the late-time behavior, particularly for the heterogeneous case which produces markedly greater retardation.

The results at late time show that the solute diffusing into the matrix adjacent to the flowing fractures (Figures 6-11 & 6-13) penetrates only a short distance as the main solute pulse passes. Therefore this solute returns to the flowing fractures relatively rapidly. Solute that enters the stagnant branches (Figure 6-12 & 6-14) and then diffuses into the adjoining matrix takes longer to return to the flowing fractures.

In the synthetic case with heterogeneous properties, the network with stagnant branch fractures actual produces less net retardation, when matrix diffusion is included, than when branch fractures are excluded. The percentiles in Table 6-4 show that the earliest 25% of mass arrival is retarded relative to the same mass fraction in the case without stagnant branches. However, later-arriving fractions of the mass are apparently less strongly retarded in the case that includes stagnant branches. This surprising behavior may be explained by the role of heterogeneity and its interaction with matrix diffusion.

In the heterogeneous version of the synthetic model that the fractures in the en échelon steps have lower transmissivity than the en échelon segments, but the pore volume per transport distance is higher than in en échelon segments. The result is that the stepovers become low-velocity zones relative to the en échelon segments.

The lower advective velocity implies more time for interaction with the matrix, and hence greater depths of matrix diffusion occur adjacent to these segments. This is seen in

Figures 6-13 and 6-14 as clouds of red dots representing solute in the matrix adjoining the stepovers. In Case AD+M (no branch fractures), this solute only returns to the flowing fractures by backward diffusion. However, in Case AD+B+M (with branch fractures), favorably positioned branch fractures provide additional pathways by which solute can return to the flowing fractures, downstream of the low-velocity steps.

These branch fractures are stagnant but have large pore volumes and high diffusivities relative to the matrix. Hence they can act as additional low-concentration boundaries for leaching of solute from the matrix just downstream of echelon steps, after the peak concentration has passed via the mobile water (flowing fractures). Since the flow past these branches is relatively rapid, they have less impact as paths for diffusion into the matrix, than as paths for release of solute that entered the matrix from adjoining, low-velocity portions of the network.

The net effect is marginal, since in either case retardation is dominated by the slow rate of diffusion into and out of matrix adjoining low-velocity portions of the network. However, for some fraction of the mass, this can reduce the delay due to matrix diffusion. Short-circuiting of the network by through-diffusion only occurs for the mass fraction of solute that experiences relatively large diffusion depths, and hence larger retention times. Hence the "accelerating" effect of through-diffusion to favorably located branch fractures is only seen in the later-arriving mass fraction (exemplified by t_{50} and higher percentiles). The mass fraction that experiences smaller diffusion depths is not subject to through-diffusion. Hence the main effect of the branch fractures for this fraction (exemplified by t_{25} and lower percentiles) is additional retardation as expected in view of the additional porosity.

The longest-retained mass fraction reflects the largest diffusion depths. These depths are attained by diffusion nominally perpendicular to the strike of the echelon zone, since solute can diffuse for effectively unbounded distances in this direction, without encountering branch fractures of the flowing network. Long branch fractures perpendicular to the strike of the zone can accentuate the retardation of the longest-retained mass fraction, by acting, in effect, as sources for radial-geometry diffusion into the matrix far from the main echelon segments. In contrast, solute traveling through a network without such fractures can only reach this region by slab-geometry diffusion. Thus the tails of the breakthrough curve (represented by t_{95} and higher percentiles) are retarded more for the case with branches than without.

A corollary to the above is that densely spaced, short "comb" cracks adjoining relatively high-velocity flowing fractures have only minor effects on the breakthrough curve (for the case of a solute pulse as considered here). Diffusion depths associated with such fractures are, on average, relatively small due to rapid passage of the concentration peak in the flowing fractures. The main expected effect is a small delay at early times. At longer time scales, interference between adjacent comb cracks results leads to slab-geometry diffusion similar to that from a simple fracture without comb cracks; the only difference is the increased pore volume.

The stagnant branches may be viewed as contributing a component of porosity additional to that considered as part of the matrix porosity θ_m. For the synthetic model, the effective porosity of the first-order stagnant branches at their intersection with the flowing fractures is $\theta_B = P_{10}\, b$, where P_{10} is the one-dimensional intensity measure of branch fractures and b is the mean aperture. For these simulations $P_{10} = 36$ m $^{-1}$ and $b = 2\text{x}10^{-4}$ m, giving $\theta_B = 0.0072$. The total effective matrix porosity seen by solute passing through the flowing fractures $\theta_m + \theta_B = 0.0122$, or a factor of 2.44 times the value of θ_m that was assumed for the matrix alone.

The applicability of standard values of matrix porosity for a model that includes centimeter-scale branch fractures might be questioned, since the length of these fractures approaches the dimension of samples used in through-diffusion experiments (*e.g.*, as reviewed by Ohlsson and Neretnieks, 1995). Conceivably some fraction of θ_B might be included in estimates of intact matrix porosity θ_m. However, core samples taken from rock that is free of through-going fractures should be mostly free of secondary fractures (given the approximately exponential decrease of secondary fracture intensity with distance from primary fractures, as noted in this research). Estimates of θ_m obtained by fitting data to in-situ tracer experiments in natural fractures are more likely to include porosity belonging to θ_B.

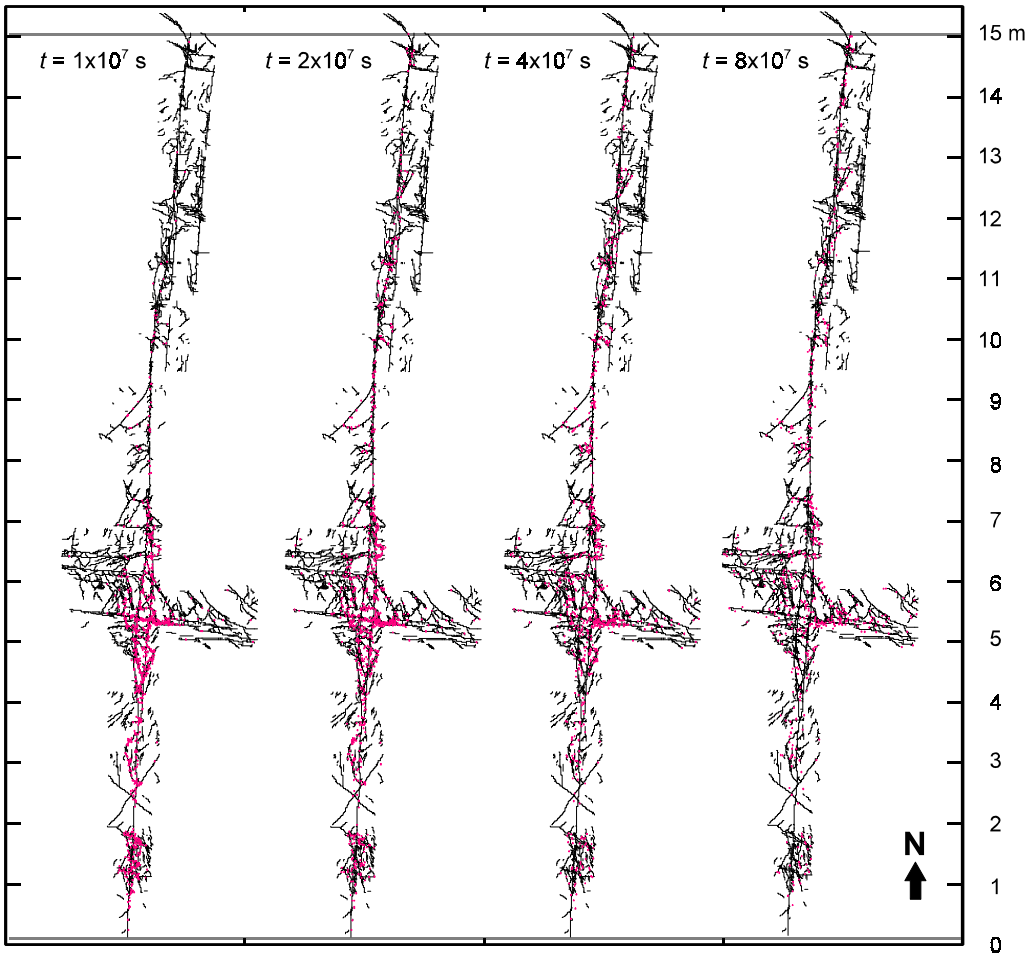

Figure 6-10. Solute distribution along 15 m long en échelon zone map at times ranging from $1x10^7$ s to $8x10^7$ s, Case ADBM (matrix diffusion with diffusion into stagnant branches). Red symbols indicate locations of particles, each representing a fixed mass of solute, at the indicated times.

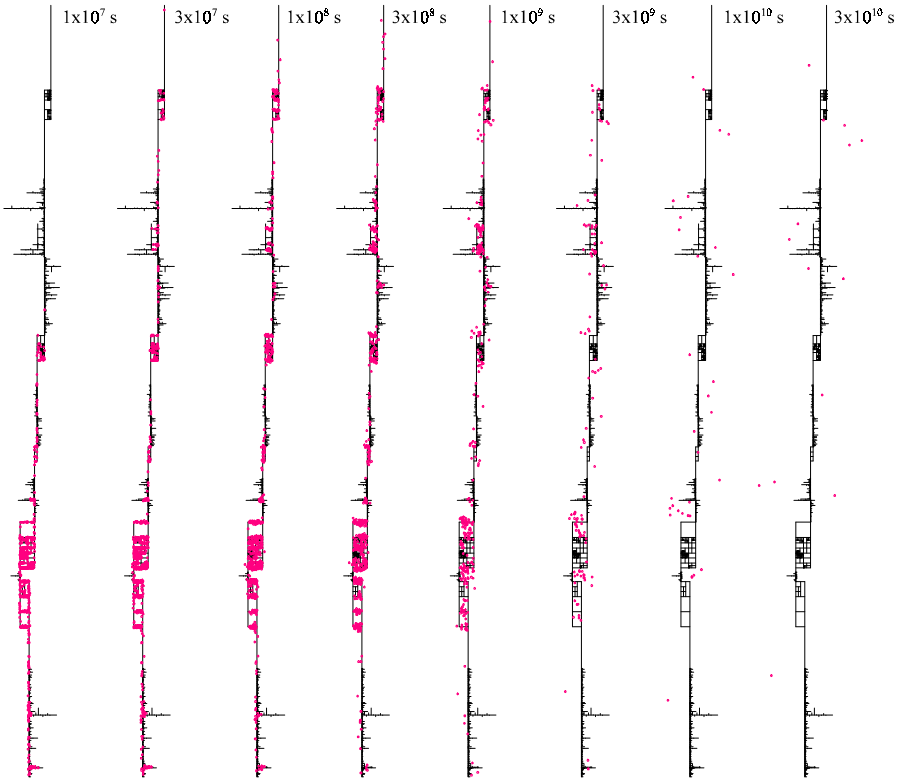

Figure 6-11. Solute distribution along 40 m long synthetic en échelon zone (uniform case) at times ranging from $1x10^7$ s to $8x10^8$ s, Case ADM (matrix diffusion without diffusion into stagnant branches). Red symbols indicate locations of particles, each representing a fixed mass of solute, at the indicated times.

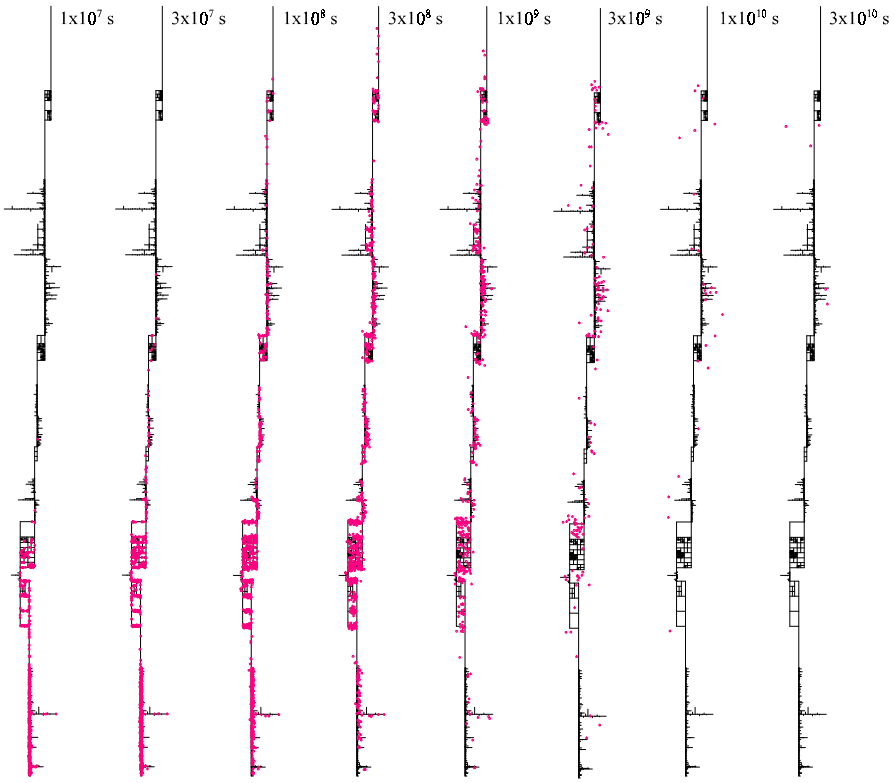

Figure 6-12. Solute distribution along 40 m long synthetic en échelon zone (uniform case) at times ranging from $1x10^7$ s to $8x10^8$ s, Case ADBM (matrix diffusion with diffusion into stagnant branches). Red symbols indicate locations of particles, each representing a fixed mass of solute, at the indicated times.

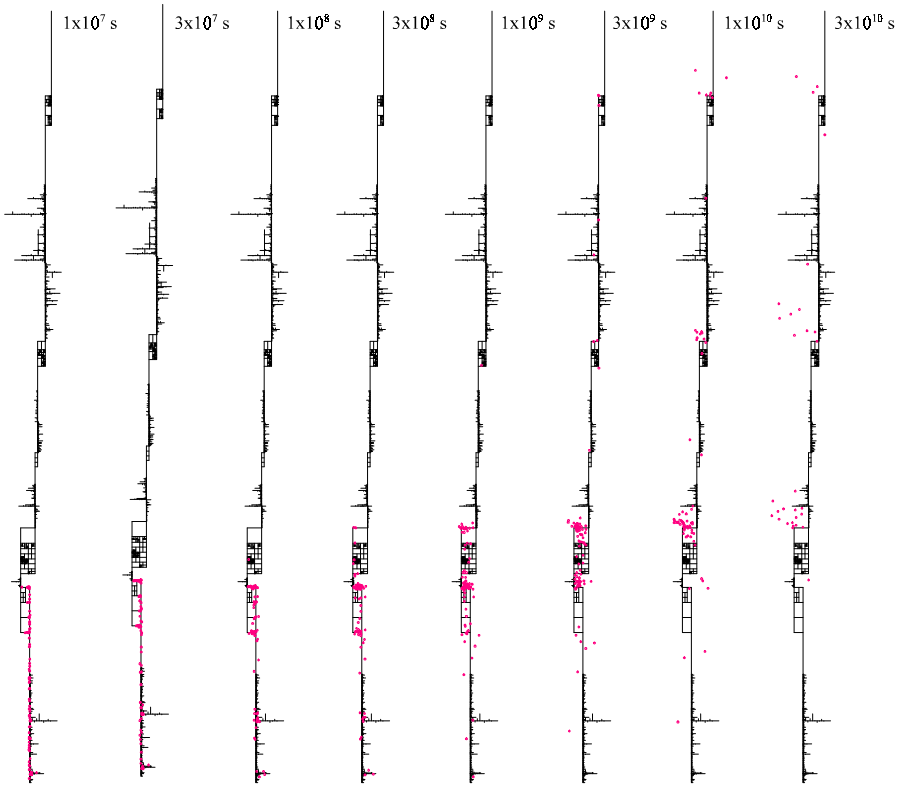

Figure 6-13. Solute distribution along 40 m long synthetic en échelon zone (heterogeneous case) at times ranging from $1x10^7$ s to $8x10^8$ s, Case ADM (matrix diffusion without diffusion into stagnant branches). Red symbols indicate locations of particles, each representing a fixed mass of solute, at the indicated times. Note that the number of particles in this simulation was about a factor of ten lower than for the corresponding (uniform) case in Figure 6-11.

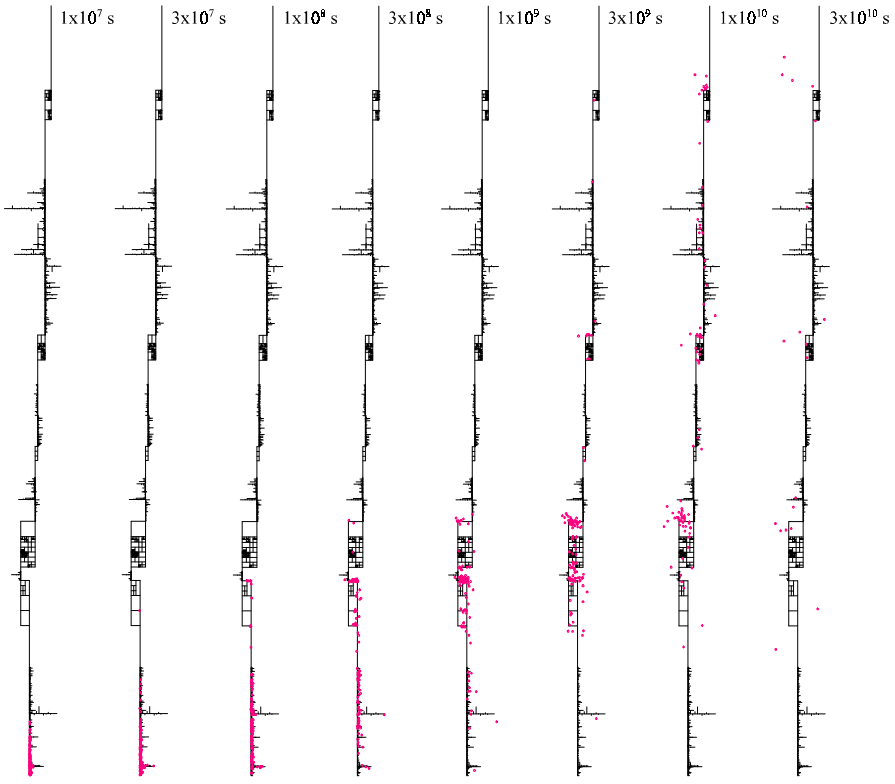

Figure 6-14. Solute distribution along 40 m long synthetic en échelon zone at times ranging from $1x10^7$ s to $8x10^8$ s, Case ADBM (matrix diffusion with diffusion into stagnant branches). Red symbols indicate locations of particles, each representing a fixed mass of solute, at the indicated times. Note that the number of particles in this simulation was about a factor of ten lower than for the corresponding (uniform) case in Figure 6-12.

6.4 Conclusions

Results are presented for models of advective-diffusive transport through en échelon fault zones, taking into account diffusion into both stagnant branch fractures and macroscopically unfractured matrix. Models analyzed include both a deterministic model based on an actual fracture map, and a synthetic model based on statistics of the 2-D geometry of en échelon zones observed at the Äspö site. The deterministic model assumes uniform hydraulic properties in all fracture segments. Two different cases of the synthetic model are analyzed, one with uniform hydraulic properties as in the deterministic model, and the second with heterogeneous properties, by which is meant lower values of transmissivity and aperture in higher-order branches.

For both models, diffusion into stagnant branches of the main en échelon segments is shown to produce up to a factor-of-two retardation of solute, relative to simple advective-diffusive transport through the main en échelon segments in the absence of matrix diffusion. The retardation is less than would be predicted by a two-domain model with equilibrium mass transfer between the flowing and stagnant domains, based on the ratio of the total pore volumes of the stagnant branch fractures and the main en échelon segments. Tailing of the simulated breakthrough curves also indicates non-equilibrium mass transfer.

The stagnant domain associated with branch fractures amounts to an additional type of immobile domain, beyond other hypothesized immobile zones (including stagnant pools in channelized fractures and stagnant fluid in gouge or breccia) which have been suggested to explain results of in situ tracer experiments. The potential for such a domain is supported by geometric evidence observed directly on outcrops.

When effects of matrix diffusion are included in the models, stagnant branches are demonstrated to enhance the retardation of solute due to matrix diffusion (in the cases with uniform hydraulic properties), and to increase the degree of late-time tailing. However, matrix diffusion is the dominant effect in terms of median arrival times for solute mass, at least for the head gradients, matrix porosities, and matrix diffusivities representative of a repository in granitic host rock that were considered in these calculations cases.

In the case with heterogeneous fracture properties, a surprising result is obtained, with branch fractures leading to slightly lower net retardation when combined with matrix diffusion. Inspection of the results indicates this may be explained as a combination of the

influence of flow-field heterogeneity on the depth of matrix diffusion, together with through-diffusion across fracture blocks. Where through-diffusion occurs, in some instances branch fractures may act as relatively rapid paths for solute to return to the flowing fractures.

From a practical standpoint in the context of a radioactive-waste repository, the principal concern with en échelon zones is that they pose a relatively well-connected, low-porosity, and potentially high-transmissivity type of pathway for transport of radionuclides, with relatively little interfacial area for exchange of solute with the matrix rock. The results presented here suggest that secondary fractures associated with such features are of net benefit in terms of radionuclide retention, but are not sufficient to mitigate those concerns significantly, either directly by providing additional immobile pore volume, or indirectly by improving access of solute to the matrix. For flow in heterogeneous networks, secondary fractures may in some circumstances accelerate breakthrough of a fraction of the solute mass by enhancing through-diffusion, although this effect is minor in the one calculation case where it is seen.

Branch fractures do apparently have the potential to affect tailing of breakthrough curves, which may be important to recognize in the interpretation of in-situ tracer experiments. If not recognized, tailing behavior due to branch fractures and branching networks of finite extent could conceivably lead to incorrect assessment of parameters for matrix diffusion models based on more simplistic diffusion geometries.

7. Significance of En échelon-zone architecture for radioactive waste disposal

Previous research reviewed here (Chapter 2) indicates that en échelon fault zones are a potentially important class of geologic features for radioactive waste disposal. As discrete structures that are well connected via more highly fractured zones at en échelon steps, they form potential flow paths over distances of tens to possibly hundreds of meters. As the en échelon segments have relatively low interfacial area, en échelon zones also have low capacity for exchange of radionuclides with the rock matrix (protolith), via matrix diffusion with or without sorption. These are the most important processes for retention of radionuclides in granitic bedrock, in the event that engineered barriers in a repository begin to leak.

The significance of en échelon zones is not strictly limited to the function of the bedrock as a barrier for radionuclides released from failed engineered barriers. A low potential for radionuclide retention due to interactions with the rock matrix also implies a relatively low potential for buffering and mixing of infiltrating groundwater of undesirable chemistry, *e.g.* oxygenated glacial meltwaters as proposed by Glynn and Voss (1996), and/or other types of groundwater that may have deleterious effects on engineered barriers such as the bentonite buffer and backfill used in the Swedish and Finnish repository concepts. These aspects have not been explored in the current dissertation. However, they may be equally important, or more important, than the properties of en échelon zones for radionuclide migration, given the importance ascribed to geochemical stability and engineered barrier longevity in recent safety assessments (SKB, 1999).

The discrete nature of en échelon segments also makes en échelon zones difficult to detect in the vicinity of a radioactive-waste repository. The anomalies for geophysical methods such as seismic reflection/refraction, magnetic, resistivity, or electromagnetic methods are likely to be less pronounced than the corresponding anomalies for distributed-deformation fault zones with high degrees of alteration. When intersected in an exploration borehole, an en échelon zone may appear to be merely a single fracture. As such it may not be recognized as a significant hydrological feature, particularly if the borehole intersects it in a relatively low-transmissivity portion of the zone.

The field investigations and analysis described in Chapters 3 and 4 provide new information on the heterogeneity of en échelon zones in granitic rock. Results suggest that a

geostatistical model may be adequate for describing the potential variation of hydraulic properties (here inferred from fracture intensity data) on scales of up to 10 m, similar to the spacing and length of en échelon steps. However, on larger scales of 50 m to 150 m, this study did not find evidence of spatial correlations in the geostatistical sense.

Systematic variations in fracture intensity correlated to structure along en échelon zones may be obscured in a geostatistical analysis, if the spacing and length of en échelon steps are variable. As a simple illustration, we may consider an ideal case in which the spacing and length of en échelon steps are constant with respect to position along strike, and fracture intensity takes on either of two values: P_1 if within one of the steps, or P_2 if between the steps. Such a model has periodic variation of fracture intensity, with period corresponding to the step spacing *S*, and correspondingly a decreased variogram at separation distances equal to integral multiples of *S*, *i.e.* what is referred to as a "hole effect" in geostatistical analysis. Next, if we consider a combined analysis of several such zones, each with a different step spacing *S*, we note that the variogram obtained by superposition will reflect interfering "hole effects" at the different values of *S*. Thus actual correlations of fracture intensity to structural features can be obscured in a conventional geostatistical analysis, if the scales of these features are variable.

To explore the consequences of systematic variations in fracture intensity correlated to structure along en échelon zones, which might not be fully characterized by a geostatistical analysis, simulations of solute transport have been performed using both actual maps and a synthetic structural model of en échelon zones. The results of these simulations are given in Chapter 6.

Analysis of detailed maps in Chapters 4 and 5 point to several characteristics that may be significant for flow and transport modeling. Fracture frequency generally decreases with distance from the median surface defined by the main en échelon segments, a characteristic common to other types of fault zones as reviewed in Chapter 2. This implies that effective hydraulic conductivity is not uniform across the nominal thickness of such zones. This has potential consequences for solute transport in that zones of varying mobility may occur in parallel within the zone. The need for more complex models to represent transport in such features in granitic rock has been recognized in recent years (Poteri *et al.*, 2002; Tsang and Doughty, 2004).

Secondary fractures (here treated as a non-genetic category encompassing splays,

wing cracks, pinnate fractures, comb cracks, *etc*.) are found to have a hierarchical branching structure, which accounts for a major portion of the elevated fracture intensity near the median surface. Thus the elevated fracture frequency adjacent to the main slip surfaces, as noted above, is not haphazardly random, but rather is organized in structural patterns that may have consequences for transport (as explored in Chapters 5 and 6).

In terms of repository safety, observations of hierarchical branches of en échelon zones pose a particular concern with respect to the concept of "respect distances" for waste emplacement. Branch fractures may provide direct connections to flowing fault zones that may not readily be recognized by methods for checking the suitability of emplacement locations. The branching structures identified here are of modest extent, and may not be of great concern in themselves. However, in view of observations such as by Kim *et al.* (2004) of structural similarity of fault zones over a very large range of scales, the possibility of large-scale branching structures than observed here should be considered.

Branch fractures in an en échelon zone could potentially act as positive attributes for repository safety. They potentially provide access to a much larger volume of rock that can react with radionuclides traveling along the zone, than would be the case for zone composed only of the primary fractures. This would imply a greater capacity for a retardation of solutes due to matrix diffusion and sorption.

A major aim of the numerical simulations in Chapter 6 was to evaluate the potential significance of branch fractures in this respect. Results indicate that, at best, branch fractures provide an additional degree of retardation which is minor relative to the effect of matrix diffusion. Their influence in this respect appears to be sensitive to groundwater velocities and heterogeneity of hydraulic properties within the fractures comprising the en échelon zone.

A surprising result of network simulations in Chapter 6 was that, in some circumstances, branch fractures apparently reduce the net retardation. This appears to be a consequence of branch fractures, in conjunction with through-diffusion under conditions of diffusion-dominated transport. Under these circumstances, branch fractures may provide relatively high-diffusivity paths by which solute can exit the immobile zone (matrix) after passage of the peak concentration. This effect is, at most, a minor factor relative to the dominant process of matrix diffusion.

The overarching conclusion, with regard to secondary fractures of en échelon zones, is that these do not provide significant additional retardation capacity, for transport scenarios

representative of post-closure repository conditions. Branching structures do not significantly mitigate the concern that en échelon zones will act as pathways with relatively low capacity for radionuclide retention in the bedrock. Thus en échelon zones must still be regarded as features with potentially negative consequences for repository safety.

On the other hand, branching structures are shown to affect the shape of solute breakthrough curves, particularly tailing phenomena. The effects of en échelon zone structure may be important for interpreting tracer tests that are conducted as part of site characterization for repositories. As shown in Chapter 5, late-time tails observed in tracer tests in-situ at the Äspö Hard Rock Laboratory can be explained in terms of diffusion into hierarchical branching structures, as mapped on an outcrop within half a kilometer of the in-situ experiments.

An important caveat on all of these conclusions is that they rely primarily on fracture geometry as observed in the plane of the given cross-sections, and on an assumption that water and solutes have equal access to all of the fractures. In reality some fractures may be entirely sealed by fracture mineralization, and other fractures are likely open to flow and solute transport over only a fraction of their extent. The three-dimensional nature of en échelon zones is evident in some of these exposures, but has not been addressed quantitatively. Gouge, fracture mineralogy, microstructure, and other properties not explored here may also affect échelon-zone transport properties. This research effort has aimed to investigate the flow and transport consequences of échelon-zone geometry, as revealed by (mainly) 2-D exposures. Other aspects of these structures certainly warrant further research.

BIBLIOGRAPHY

Note: This bibliography follows American conventions for alphabetical order, treating letters with diacritical marks (ä, å, and ö) as equivalent to the letters without such marks. The author apologizes for any inconvenience to readers who may expect to find these letters alphabetized after z.

Abelin, H., L. Birgersson, H. Widén, T. Ågren, L. Moreno, and I. Neretnieks, 1990. Channeling Experiment, Stripa Project Technical Report 90-13, Swedish Nuclear Fuel and Waste Management Co., Stockholm.

Abelin, H, I. Neretnieks, S. Tunbrant, and L. Moreno, 1985. Final report of the migration in a single fracture - Experimental results and evaluation, Stripa Project Technical Report 85-03, Swedish Nuclear Fuel and Waste Management Co., Stockholm.

Ahlstrom, S. W., Foote, H. P., Arnett, R. C., Cole, C. R., and Serne, R.J., 1977. Multicomponent mass transport model. Theory and numerical implementation (discrete parcel random walk version), Battelle report BNWL for ERDA, Columbus, Ohio.

Anderson, J. G. C., 1978. *The Structure of Western Europe*, Pergamon Press, Oxford, 250 p.

Anderson, L. J., Osborne, R. H., and Palmer, D. F., 1983. Cataclastic rocks of the San Gabriel fault – An expression of deformation at deeper crustal levels in the San Andreas fault zones. *Tectonophysics*, v. 98, p. 209-251.

Andersson, J-E, L. Ekman, E. Gustafsson, R. Nordqvist, and S. Tirén, 1989a. Hydraulic interference tests and tracer tests within the Brändan area, Finnsjön study site -- The Fracture Zone Project -- Phase 3, SKB Technical Report 89-12, Swedish Nuclear Fuel and Waste Management Co., Stockholm.

Andersson, J-E, L. Ekman, R. Nordqvist, and A. Winberg, 1989b. Hydraulic testing and modeling of a low-angle fracture zone at Finnsjön, Sweden. In SKB Technical Report 89-19, Swedish Nuclear Fuel and Waste Management Co., Stockholm

Andersson, J-E, Nordqvist, R, Nyberg, G, Smellie, J, and Tirén, S, 1991. Hydrogeological conditions in the Finnsjön area: Compilation of data and conceptual model, SKB Technical Report 91-24, Swedish Nuclear Fuel and Waste Management Co., Stockholm.

Andersson, J., and Dverstorp, B., 1987. Conditional simulations of fluid flow in three-dimensional networks of discrete fractures. *Water Resources Research*, v. 23, p. 1876-1886.

Antonellini, M. and Aydin, A., 1994. Effect of faulting on fluid flow in porous sandstones: Petrophysical properties. *American Association of Petroleum Geologists Bulletin*, v. 78, p. 355-377.

Aris, R., 1956. On the dispersion of solute in a fluid moving through a tube. *Proceedings of the Royal Society of London Ser. A*, v. 235, p. 67-77.

Aydin, A., 1978. Small faults formed as deformation bands in sandstone. *Pure Appl. Geophysics* v. 116:913-930.

Aydin, A., and Nur, A., 1985. The types and role of stepovers in strike-slip tectonics. *Society of Economic Paleontologists and Mineralogists Special Publication No. 37*, p. 35-44.

Aydin, A. and Schultz, R.A., 1990. Effect of mechanical interaction on the development of strike-slip faults with echelon patterns. *Journal of Structural Geology*, v.12, p.123-129.

Bäckblom, G., and Karlsson, F., 1990. Swedish programme for disposal of radioactive waste – geological aspects. *Geologiska Föreningens I Stockholm Förhandlingar*, v. 112, p. 307-315.

Bandis, S., A.C. Lumisden, and N.R. Barton, 1981. Experimental studies of scale effects on the shear behaviour of rock joints, *Int. J. Rock Mechanics, Mining Science and Geomechanics Abstracts* v. 18, p. 1-21.

Bandis, S., A.C. Lumisden, and N.R. Barton, 1983. Fundamentals of rock joint deformation, *Int. J. Rock Mechanics, Mining Science and Geomechanics Abstracts* v. 20, p. 249-268.

Barton, C.A., Zoback, M.D. and Moos, D., 1995. Fluid flow along potentially active faults in granitic bedrock. *Geology*, v. 23, p. 683-686.

Barton, N., Bandis, S., and Bakhtar, K., 1985. Strength, deformation and conductivity coupling of rock joints. *International Journal of Rock Mechanics, Mineral Science and Geomechanics Abstracts*, v. 22, p.121-140.

Bates, R.L. and Jackson, J.A., eds., 1984. *Dictionary of Geologic Terms*, 3rd edition, American Geological Institute.

Bear, J., 1993. Modeling flow and contaminant transport in fractured rocks. *In* Bear, J., Tsang, C-F, and de Marsily, eds., *Flow and Contaminant Transport in Fractured Rock*, Academic Press, San Diego, p. 1-35.

Bergman, T., Isaksson, H., Johansson, R., Lindén, A. H., Lindgren, J., Lindroos, H., Rudmark, I., and Wahlgren, C.-H.., 1998. *Förstudie Oskarshamn. Jordarter, bergarter och deformationszoner* (Pre-study Oskarshamn: Soil types, rock types, and deformation zones), SKB Report R-98-56, Swedish Nuclear Fuel and Waste Management Co., Stockholm.

Berkowitz, B., Nauman, C., and Smith, L., 1994. Mass transfer at fracture intersections: An evaluation of mixing models. *Water Resources Research*, v. 30, p. 1765-1773.

Biegel, R. L., Sammis, C. G., and Dieterich, J. H., 1989. The frictional properties of simulated fault gouge having a fractal particle distribution. *Journal of Structural Geology*, v. 11, p. 827-846.

Billaux, D., Chiles, J. P., Hestir, K., and Long, J. C. S., 1989. Three-dimensional statistical modeling of a fractured rock mass – an example from the Fanay-Augeres Mine. *International Journal of Rock Mechanics, Mining Science and Geomechanics Abstracts*, v. 26, p.281-299.

Bjarnasson, B. and Stephansson, O., 1988. Hydraulic fracturing stress measurements in the borehole Fi 06, Finnsjön. SKB Working Report R&D 88-54, Swedish Nuclear Fuel and Waste Management Co., Stockholm.

Bour, O. and Davy, P., 1997. Connectivity of random fault networks following a power law length distribution, *Water Resources Research*, v. 33, p. 1567-1583.

Bourke, P. T., 1987. Channeling of flow through fractures in rock, *in* Proceedings of the GEOVAL-87 International Symposium, Stockholm, April 7-9, 1987.

Brace, W.F., 1960. An extension of Griffith theory of fracture to rocks, *Journal of Geophysical Research*, v. 65, p. 3477-3480.

Brown, A., Everitt, R.A., Martin, C.D., and Davison, C.C., 1995. Past and future fracturing in AECL research areas in the Superior province of the Canadian Precambrian Shield, with emphasis on the Lac du Bonnet Batholith. Atomic Energy of Canada Ltd. Report AECL-11214, COG-94-528, Whiteshell Laboratories, Pinawa, Manitoba.

Brown, S. R., 1987. Fluid flow through rock joints: The effect of surface roughness, *Journal of Geophysical Research*, v. 92, 1337-1347.

Brown, S. R., Kranz, R. L. and Bonner, B. P. 1986. Correlation between the surfaces of natural rock joints, *Geophysical Research Letters*, v. 13, p. 1430-1434.

Brown, S. R. and Scholz, C. H., 1985. Broad bandwidth study of the topography of natural rock surfaces, *Journal of Geophysical Research*, v. 90, p. 12,575-12,582.

Brown, S. R. and Scholz, C. H., 1986. Closure of rock joints, *Journal of Geophysical Research*, v. 91, p. 4939-4948.

Brown, S.R., Stockman, H.W., and Reeves, S. J., 1995. Applicability of the Reynolds equation for modeling fluid flow between rough surfaces, *Geophysical Research Letters*, v. 22, p. 2537-2540.

Bruderer, C. and Bernabé, Y., 2001. Network modeling of dispersion: Transition from Taylor dispersion in homogeneous networks to mechanical dispersion in very heterogeneous ones. *Water Resources Research*, v. 37, p. 897-908.

Bruhn, R. L., Yonkee, W. E., and Parry, W. T., 1994. Structural and fluid-chemical properties of seismogenic normal faults, *Tectonophysics*, v.175, p.139-157.

Byerlee, J., 1993. Model for episodic flow of high-pressure water in fault zones before earthquakes. *Geology*, v. 21, p. 303-306

Cacas, M. C., Ledoux, E., de Marsily, G., Tillie, B., Barbreau, A., Durand, E., Fuega, B. and Peaudecerf, P., 1990a. Modeling fracture flow with a stochastic discrete fracture network: Calibration and validation, 1, The flow model. *Water Resources Research*, v. 26, p. 479-489.

Cacas, M.C., Ledoux, E., de Marsily, G., Barbreau, A., Calmels, P., Gaillard, B. and Margritta, R., 1990b. Modeling fracture flow with a stochastic discrete fracture network: Calibration and validation, 2, The transport model. *Water Resources Research*, v. 26, p. 491-500.

Caine, J. S., 1999. The architecture and permeability structure of brittle fault zones. Ph.D. thesis, Department of Geology and Geophysics, University of Utah, 134 p.

Caine, J. S., Coates, D. R., Timoffeef, N. P., and Davis, W. D., 1991. Hydrogeology of the Northern Shawangunk Mountains. New York State Geological Survey Open-File Report 1g806, 72 p. and maps.

Caine, J. S., Evans, J. P., and Forster, C. B., 1996. Fault zone architecture and permeability structure, *Geology*, v. 24, p. 1025-1028.

Caine, J. S. and Forster, C. B., 1999. Fault zone architecture and fluid flow: Insights from field data and numerical modeling. In Haneberg, W.C., Mozley, P.S., Moore, J.C., and Goodwin, L.B., *Faults and Subsurface Fluid Flow in the Shallow Crust*, AGU Geophysical Monograph, v. 113, p. 107-127.

Carlsson, A., and Olsson, T., 1986. Large scale in-situ tests on stress and water flow relationships in fractured rock. RD&D report, Vattenfall AB, Vällingby, Sweden.

Chester, F. M. and Chester, J.S., 1998. Ultracataclasite structure and friction processes of the Punchbowl fault, San Andreas system, California. *Tectonophysics*, v. 295, p.199-222.

Chester, F. M., Evans, J. P., and Beigel, R. I., 1992. Internal structure and weakening mechanisms of the San Andreas Fault. *Journal of Geophysical Research*, v. 98, p.778-786.

Chester, F. M. and Logan, J. M., 1986. Composite planar fabric of gouge from the Punchbowl fault, California. *Journal of Structural Geology*, v. 9, p. 621-634.

Childs, C., Nicol, A., Walsh, J. J., and Watterson, J., 1996a. Growth of vertically segmented normal faults. *Journal of Structural Geology*, v. 18, p.1389-1397.

Childs, C., Watterson, J., and Walsh, J. J., 1996b. A model for the structure and development of fault zones. *J. Geological Society*, v. 153, p. 337-340.

Clemo, T., 1994. Dual permeability modeling of fractured media. Ph. D. thesis, University of British Columbia, Vancouver.

Committee on Fracture Characterization and Fluid Flow, U.S. National Committee for Rock Mechanics, and Geotechnical Board, Board on Energy and Environmental Systems, Commission on Engineering and Technical Systems, National Research Council, 1996. *Rock Fractures and Fluid Flow*, National Academy Press, Washington D.C., 551 p.

Cooke, M. L., 1997. Fracture localization along faults with spatially varying friction. *Journal of Geophysical Research*, v. 102(B10), p. 22,425-22,434.

Cruikshank, K. M., Zhao, G., and Johnson, A. M., 1991a. Analysis of minor fractures associated with joints and faulted joints. *Journal of Structural Geology*, v.13(8), p.865-886.

Cruikshank, K. M., Zhao, G., and Johnson, A. M., 1991b. Duplex structures connecting fault segments in Entrada sandstone. *Journal of Structural Geology*, v.13(8), p.1185-1196.

Cunningham, J. A. and Roberts, P. V., 1998. Use of temporal moments to investigate the effects of nonuniform grain-size distribution on the transport of sorbing solutes. *Water Resources Research*, v. 34(6), p.1415-1425.

Davison, C. C. and Kozak, E. T., 1988. Hydrogeologic characteristics of major fracture zones in a large granite batholith of the Canadian shield. In *Proceedings of the 4th Canadian-American Conference on Hydrogeology*, Banff, June 1988. Published by National Ground Water Association, Dublin, Ohio.

Delay, F. and Bodin, J., 2001. Time domain random walk method to simulate transport by advection-dispersion and matrix diffusion in fracture networks. *Geophysical Research Letters*, v. 37(10) p. 2503-2512.

Di Pietro, L. B., 1996. Application of a lattice-gas numerical algorithm to modeling water transport in fractured media, *Transport in Porous Media*, v. 22, p. 307-325.

Dershowitz, W. S., *Rock Joint Systems*, Ph.D. dissertation, Massachusetts Institute of Technology, 1984.

Dershowitz, W. S. and Herda, H. H., 1992. Interpretation of fracture spacing and intensity. In Tillerson, J.R. and Wawersik, W.R. (eds.), *Rock Mechanics: Proceedings of the 33rd U.S. Symposium*, Santa Fe, New Mexico 3-5 June 1992, Balkema, Rotterdam, p. 757-766.

Dershowitz, W. S., Lee, G., Geier, J., Foxford, T., LaPointe, P., and Thomas, A., 1996. FracMan™: Interactive discrete feature data analysis, geometric modeling, and exploration simulation: User Documentation, Version 2.5, Golder Associates Inc., Redmond, Washington.

Dershowitz, W. S. and Miller, I., 1995. Dual porosity fracture flow and transport, *Geophysical Research Letters*, v. 22, p. 1441-1444.

Dershowitz, W. S., Wallman, P., and Kindred, S., 1991. Discrete fracture modeling for the Stripa site characterization and validation experiment. Stripa Project Technical Report 91-16, Swedish Nuclear Fuel and Waste Management Co., Stockholm.

Detwiler, R. L., Rajaram, H., and Glass, R. J., 2000. Solute transport in variable-aperture fractures: An investigation of the relative importance of Taylor dispersion and macrodispersion, *Water Resources Research* v. 36(7), p. 1611-1625.

de Dreuzy, J.-R., Davy, P., and Bour, O., 2001a. Hydraulic properties of two-dimensional fracture networks following a power law length distribution: 1. Effective connectivity. *Water Resources Research*, v. 37(8), p. 2065-2078.

de Dreuzy, J.-R., Davy, P., and Bour, O., 2001b. Hydraulic properties of two-dimensional fracture networks following a power law length distribution: 2. Permeability of networks based on a lognormal distribution of apertures. *Water Resources Research*, v. 37(8), p. 2079-2095.

Du, Y., and Aydin, A., 1991. Interaction of multiple cracks and formation of echelon crack arrays, *International Journal of Numerical and Analytical Methods in Geomechanics*, v. 15(3), p. 205-218.

Du, Y. and Aydin, A., 1993. The maximum distortional strain energy density criterion for shear fracture propagation with applications to the growth paths of *en échelon* faults, *Geophysical Research Letters*, v. 20(11), p.1091-1094.

Dverstorp, B., Andersson, J., and Nordqvist, W., 1992. Discrete fracture network interpretation of field tracer migration in sparsely fractured rock, *Water Resources Research*, v. 28(9), p. 2327-2343.

Dverstorp, B., Geier, J., and Voss, C., 1996. Simple evaluation of groundwater flow and radionuclide transport at Äspö. SKI Report 96:14, Swedish Nuclear Power Inspectorate, Stockholm.

Elsworth, D., and Doe, T. W., 1986. Application of nonlinear flow laws in determining rock fissure geometry from single borehole pumping tests. *Int. J. Rock Mech. Min. Sci. & Geomech. Abstr*., v. 23(3), p. 245-254.

Endo, H. K., Long, J. C. S., Wilson, C. R., and Witherspoon, P. A., 1984. A model for investigating mechanical transport in fracture networks. *Water Resources Research*, v. 20(10), p. 1390-1400.

Ericsson, L. O., 1987. Fracture mapping on outcrops. Äspö. SKB Swedish Hard Rock Laboratory Progress Report 25-87-05, Swedish Nuclear Fuel and Waste Management Co., Stockholm.

Evans, J. P., Forster, C. B., and Goddard, J. V., 1997. Permeability of fault-related rocks and implications for hydraulic structure of fault zones. *Journal of Structural Geology*, v. 19(11),p. 1393-1404.

Fairley, J., Heffner, J., and Hinds, J., 2003. Geostatistical evaluation of permeability in an active fault zone. *Geophysical Research Letters*, v. 30(18), 1962, doi:10.1029/2003GL018064.

Falconer, K., 1990. *Fractal Geometry: Mathematical Foundations and Applications.* Wiley & Sons, Chichester, UK, 288 p.

Fischer, U., Kulli, B., and Flühler, H., 1998. Constitutive relationships and pore structures of undisturbed fracture zone samples with cohesionless fault gouge layers. *Water Resources Research*, v. 34(7), p. 1695-1701.

Forster, C. B., and Evans, J. P. 1991. Impact of a permeable thrust fault on thermal and hydrologic regimes: Regional-scale numerical modeling results. *GSA Abstracts with Programs*, p. A104.

Forster, C. B., Evans, J. P., Tanaka, H., Jeffreys, R., and Nohara, T., 2003. Hydrologic properties and structure of the Mozumi Fault, central Japan. *Geophysical Research Letters*, v. 30(6), 8010, doi:10.1029/2002GL014904.

Fossen, H., and Rykkelid, E., 1992. Postcollisional extension of the Caledonide orogen in Scandinavia: Structural expressions and tectonic significance. *Geology*, v. 20, p. 737-740.

Gale, J. E., 1987. Comparison of coupled fracture deformation and fluid flow models with direct measurements of fracture pore structure and stress-flow properties. Proceedings of the 28th U.S. Rock Mechanics Symposium, Tucson, Arizona, June 29 - July 1, 1987.

Gale, J. E. and Raven, K. G., 1980. Effects of sample size on the stress-permeability relationship for natural fractures. Report LBL-11865/SAC-48/UC-70, Swedish-American Cooperative Program on Radioactive Waste Storage in Mined Caverns in Granitic Rock, Swedish Nuclear Fuel and Waste Management Co., Stockholm.

Ge, S., 1997. A governing equation for fluid flow in rough fractures. *Water Resources Research*, v. 33, p. 53-61.

Geier, J.E., 1996. Discrete-feature modelling of the Äspö site: 3. Predictions of hydrogeological parameters for performance assessment (SITE-94), SKI Report 96:7, Swedish Nuclear Power Inspectorate, Stockholm.

Geier, J.E., Axelsson, C.-L., Hässler, L., and Benabderrahmane, A., 1992. Discrete-fracture network modelling of the Finnsjön rock mass: Phase 2. SKB Technical Report 92-07, Swedish Fuel and Waste Management Co., Stockholm.

Geier, J. E., Doe, T. W., Benabderrahman, A., and Hässler, L., 1995. Generalized radial flow interpretation of well tests for the SITE-94 project. SKI Technical Report 96:4, Swedish Nuclear Power Inspectorate, Stockholm.

Geier, J. E. and Hässler, L., 1992. Scale effects in estimating fractured rock block conductivity from packer tests. In Tillerson, J.R. and Wawersik, W.R. (eds.), *Rock Mechanics: Proceedings of the 33rd U.S. Symposium*, Santa Fe, New Mexico 3-5 June 1992, Balkema, Rotterdam, p. 551-560.

Geier, J. E., Lee, K., and Dershowitz, W. S., 1988. Field validation of conceptual models for fracture geometry. American Geophysical Meeting Poster Session Abstract H12A-10 1605, *EOS*, v. 69(44), p.1177.

Geier, J. E., and Thomas, A. L., SITE-94: Development of discrete-fracture network models for repository-scale flow and transport. SKI Technical report 96:5, Swedish Nuclear Power Inspectorate, Stockholm, 1996.

Geier, J. (ed.), Tirén, S., Dverstorp, B., and Glynn, P., 1996. SITE-94: Site-specific base data for the performance assessment. SKI Report 96:10, Swedish Nuclear Power Inspectorate, Stockholm.

Gelhar, L. W., 1987. Applications of stochastic models to solute transport in fractured rocks. SKB Technical Report 87-05, Swedish Nuclear Fuel and Waste Management Co., Stockholm.

Gentier, S., 1986. Morphologie et comportment hydromechanique d'une fracture naturelle dans une granite sous constrainte normale. Ph. D. dissertation, L'Universite d'Orleans.

Gentier, S., Billaux, D., and van Vliet, L., 1989. Laboratory testing of the voids of a fracture, *Rock Mechanics and Rock Engineering*, v. 22, p. 149-157.

Glynn, P. and Voss, C., 1996. Geochemical characterization of ground waters near the Äspö Hard Rock Laboratory, Simpevarp Region, Sweden. SKI Technical Report 96:29, SKI, Stockholm.

Gorbatschev, R., 1980. The Precambrian development of southern Sweden, *Geologiska Föreningens I Stockholm Förhandlingar*, v.102, p.129-136.

Gorbatschev, R., Lindh, A., Solyom, Z., Laitikari, I., Aro, K., Lobach-Zhuchenko, S.B., Markov, M.S., Ivliev, A.I., and Brynhi, I., 1987. Mafic dyke swarms of the Baltic shield. In Hall and Fahrig (eds.), *Mafic Dyke Swarms*, GAC Special Paper 34.

Gudmundsson, A., 1987. Tectonics of the Thingvellir fissure swarm, SW Iceland, *Journal of Structural Geology*, v. 9, p. 61-69.

Gustafson, G. 1990. Identification and nomenclature of fracture zones. In *Proceedings of the 3rd NEA/SKB Symposium on In Situ Experiments Associated with the Disposal of Radioactive Waste*, Stockholm, 3-4 October 1989, p. 218-222. Organization for Economic Cooperation and Development, Paris.

Gustafsson, E. and Nordqvist, R., 1993. Radially converging tracer test in a low-angle fracture zone at the Finnsjön site, central Sweden. The Fracture Zone Project -- Phase 3. SKB Technical Report 93-25, Swedish Nuclear Fuel and Waste Management Co., Stockholm.

Gutfraind, R. and Hansen, A.,1995. Study of fracture permeability using lattice gas automata, *Transport in Porous Media*, v. 18, p. 131-149.

Haggerty, R., 2001. Matrix diffusion: Heavy-tailed residence-time distributions and their influence on radionuclide retention, in *Radionuclide Retention in Geologic Media*, Workshop Proceedings, Oskarshamn, Sweden, 7-9 May 2001. Radioactive Waste Management GEOTRAP Project, Organization for Economic Cooperation and Development, p. 81-90.

Haggerty, R., Fleming, S. W., Meigs, L. C., and McKenna, S. A., 2001. Tracer tests in a fractured dolomite: 2. Analysis of mass transfer in single-well injection-withdrawal tests. *Water Resources Research*, v. 37(5), p. 1129-1142.

Haggerty, R. and Gorelick, S. M., 1995. Multiple-rate mass-transfer for modeling diffusion and surface reactions in media with pore-scale heterogeneity, *Water Resources Research*, v. 36(12), p. 3467-3479.

Hakami, E., 1989. Aperture measurements and flow experiments using plastic resin replicas of rock joints.

Hartikainen, J., Hartikainen, K., Hautojärvi, A., Kuoppamäki, K., and Timonen, J., 1996. Helium gas methods for rock characteristics and matrix diffusion. Posiva Oy, Helsinki, 55 p.

Hazzard, J. F. and Mair, K., 2003. The importance of the third dimension in granular shear. *Geophysical Research Letters*, v. 30(13),1708 doi:10.1029/2003GL017534.

Heath, M. J., 1984. Solute migration experiments in fractured granite, South West England, *in* Design and Instrumentation of In Situ Experiments in Underground Laboratories for Radioactive Waste Disposal; Proceedings of a Joint CEC-NEA Workshop, Brussels, May 15-17, 1984.

Herbert, A. W., Gale, J. E., Lanyon, G. W., and MacLeod, B., 1991. Modeling for the Stripa site characterization and validation drift inflow prediction of flow through fractured rock. Stripa Project Technical Report 91-35, Swedish Nuclear Fuel and Waste Management Co., Stockholm.

Hestir, K., Martel, S. J., Yang, J., Evans, J. P., Long, J. C. S., D'Onfro, P., and Rizer, W. D., 2001. Use of conditional simulation, mechanical theory, and field observations to characterize the structure of faults and fracture networks. *In* Evans, D.D., Nicholson, T.J., and Rasmussen, T.C., *Flow and Transport Through Unsaturated Fractured Rock*, Geophysical Monograph 42, 2nd Edition, American Geophysical Union, Washington, D.C..

Hicks, T., Wickham, S., Bruel, D., Jeong, W.-C., Connolly, P., Goelke, M., Podlachikov, Y., and Rodrigeus, N., 2000. Modeling the influence of fault zone heterogeneity and the hydrodynamics of fault movement in hydrogeological systems. European Commission Report EUR 19134.

de Hoog, F. R., Knight, J. H., and Stokes, A. N., 1982. An improved method for numerical inversion of Laplace transforms, *SIAM Journal of Scientific and Statistical Computing*, v. 3(3), p. 357-366.

Hopkins, D. L., Cook, N. G. W., and Myer, L. R., 1990. Normal joint stiffness as a function of spatial geometry and surface roughness. In *Rock Joints: Proceedings of the International Symposium on Rock Joints*, Loen, Norway, June 4-6, p. 203-210.

Hull, J., 1988. Thickness-displacement relationships for deformation zones. *Journal of Structural Geology*, v. 10, p. 431-435.

Itasca Consulting Group, UDEC User's guide, Version 3.1, Minneapolis, Minnesota, 2000.

Iwai, K., 1976. *Fundamental studies of fluid flow through a single fracture.* Ph.D. dissertation, University of California, Berkeley.

Jackson, C. P., Hoch, A. R., and Todman, S., 2000. Self-consistency of a heterogeneous continuum porous medium representation of a fractured medium. *Water Resources Research*, v. 36(1), p. 189-202.

Jaeger, J. C., and Cook, N. G. W., 1979. *Fundamentals of Rock Mechanics*, 3rd Edition, Chapman and Hall, London, 593 p.

Jakob, A., 2004. Matrix diffusion for performance assessment – Experimental evidence, modelling assumptions and open issues. PSI Bericht Nr. 04-08, Paul Scherrer Institut, Villigen, Switzerland.

Jakob, A., Mazurek, M., and Heer, W., 2003. Solute transport in granitic rocks at Äspö – II: Blind predictions, inverse modelling and lessons learnt from test STT1. *Journal of Contaminant Hydrology*, v. 61, p. 175-190.

Johansson, H., Siitari-Kauppi, M., Skålberg, M., and Tullborg, E.-L.,1998. Diffusion pathways in crystalline rock – examples from Äspö diorite and fine-grained granite. *Journal of Contaminant Hydrology*, v. 35(1-3), p. 41-53.

de Josselin de Jong, G., 1958. Longitudinal and transverse dispersion in granular deposits. Transactions of the American Geophysical Union, v. 39, p. 67-74.

Kearey, P., and Vine, F. J., *1990. Global Tectonics*. Blackwell Scientific Publications, Oxford, 203 p.

Keller, A. A., Roberts, P. V., and Blunt, M. J., 1999. Effect of fracture aperture variations on the dispersion of contaminants. *Water Resources Research*, v. 35(1), p. 55-63.

Kim, Y.-S., Peacock, D. C. P., and Sanderson, D. J., 2004. Fault damage zones. *Journal of Structural Geology*, v. 26, p. 503-517.

Kohl, T., Evans, K. F., Hopkirk, R. J., Jung, R., and Rybach, L., 1997. Observation and simulation of non-Darcian flow transients in fractured rock. *Water Resources Research*, v. 33(3), p. 407-418.

Kornfält, K.-A. and Wikman, H., 1987. Description to the map (No. 4) of solid rocks of three small areas around Simpevarp, Swedish Hard Rock Laboratory Progress Report 25-87-02a, Swedish Nuclear Fuel and Waste Management Co., Stockholm ,1987.

Kornfält, K-A. and Wikman, H., 1988. The rocks of Äspö Island: Description to the detailed maps of solid rocks including maps of 3 uncovered trenches, Swedish Hard Rock Laboratory Progress Report 25-88-12, Swedish Nuclear Fuel and Waste Management Co., Stockholm.

Kornfält, K.-A., Persson, P.-O., and Wikman, H., 1997. Granitoids from the Äspö area, southeastern Sweden – geochemical and geochronological data, *Geologiska Föreningens I Stockholm Förhandlingar*, v. 119, p.109-114.

Krizek, R. J., Karadi, R. M., and Socias, E., 1972. Dispersion of a contaminant in fissured rock, *Proceedings of the International Society of Rock Mechanics Symposium on Percolation through Fissured Rock*, Stuttgart, Germany.

Lagerbäck, R. and Witschard, F., 1983. Neotectonics in northern Sweden – geological investigations. SKBF/KBS Teknisk Rapport TR-83-58, Swedish Nuclear Fuel and Waste Management Co., Stockholm.

Larsson, S.-Å., and E.-L. Tullborg, 1993. Tectonic regimes in the Baltic Shield during the last 1200 Ma – A review. SKB Technical Report 94-05, Swedish Nuclear Fuel and Waste Management Co., Stockholm

Lee, J.-J. and Bruhn, R. L., 1996. Structural anisotropy of normal fault surfaces. *Journal of Structural Geology*, v. 18(8), p. 1043-1059

Lee, K., 1988. Report on development and validation of conceptual models for major fracture zones, GAI report 873-1313.011, Golder Associates Inc., Redmond, Washington.

Lee, S. H., Lough, M. F., and Jensen, C. L., 2001. Hierarchical modeling of flow in naturally fractured formations with multiple length scales. *Water Resources Research*, v. 37(3), p. 443-455.

Lidmar-Bergström, K., 1991. Phanerozoic tectonics in southern Sweden. *Zeitschrift für Geomorphologie*, v. 82,p. 1-16.

Lin, P. and Logan, J. M., 1991. The interaction of two closely spaced cracks: A rock model study. *Journal of Geophysical Research*, v. 96(B13), p. 21,667-21,675.

Löfgren, M. and Neretnieks, I., Formation factor logging in-situ by electrical methods. SKB Technical Report TR-02-27, Swedish Nuclear Fuel and Waste Management Co., Stockholm.

Logan, J. M., 1992. The influence of fluid flow on the mechanical behavior of faults. In Tillerson, J.R., and Wawersik, W.R., eds., *Rock Mechanics: Proceedings of the 33rd U.S. Symposium*, p. 141-149, Balkema, Rotterdam.

Logan, J. M., Dengo, C. A., Higgs, N. G., and Wang, Z. Z., 1992. Fabric of experimental fault zones: Their development and relationship to mechanical behavior. In *Fault Mechanics and Transport Properties of Rocks*, Academic Press.

Long, J. C. S., Gilmour, P., and Witherspoon, P. A., 1985. A model for steady fluid flow in random three-dimensional networks of disc-shaped fractures. *Water Resources Research*, v. 21(8), p. 1105-1115.

Long, J. C. S., Remer, J. S., Wilson, C. R. and Witherspoon, P. A., 1982. Porous media equivalents for networks of discontinuous fractures. *Water Resources Research*, v.18(3), p. 645-658.

Long, J. C. S. and Witherspoon, P. A., 1985. The relationship of the degree of interconnection to permeability in fracture networks. *Journal of Geophysical Research*, v. 90(B4), p. 3087-3098.

López, D. L. and Smith, L., 1996. Fluid flow in fault zones: Influence of hydraulic anisotropy and heterogeneity on the fluid flow and heat transfer regime, *Water Resources Research*, v. 32(12), p. 3227- 3235.

Louis, C., 1969. A study of groundwater flow in jointed rock and its influence on the stability of rock masses. Imperial College of Rock Mechanics Report No. 10, London.

Lyakhovsky, V., Ben-Zion, Y., and Agnon, A., 1997. Distributed damage, faulting and friction. *Journal of Geophysical Research*, v.102(B12), p. 27,635-27,649.

Makurat, A., Barton, N., Tunbridge, L., and Vik, G., 1990a. The measurement of joint properties at different scales in the Stripa project, *Rock Joints: Proceedings of the International Symposium on Rock Joints*, Loen, Norway, June 4-6, p. 541-548.

Makurat, A., Barton, N., Vik, G. and Tunbridge, L., 1990b. Site characterization and validation – Coupled stress-flow testing of mineralized joints of 200 mm and 1400 mm length in the laboratory and in situ, Stage 3. Stripa Project Technical Report 90-07, Swedish Nuclear Fuel and Waste Management Co., Stockholm.

Malowszewski, P. and Zuber, A., 1985. On the theory of tracer experiments in fissured rocks with a porous matrix, *Journal of Hydrology*, v. 79, p. 333-358.

Mandelbrot, B.B., 1982. *The Fractal Geometry of Nature*, Freeman, San Francisco.

Marone, C. and Scholz, C. H.,1989. Particle-size distribution and microstructures within simulated fault gouge, *Journal of Structural Geology*, v. 11, p. 799-814.

de Marsily, G., 1986. *Quantitative Hydrogeology: Groundwater Hydrology for Engineers*, English edition translated by Gunilla de Marsily, Academic Press, Orlando, Florida, 440 p.

Martel, S. J., 1990. Development of compound fault zones in granitic rock, Mount Abbot quadrangle, Sierra Nevada, California. *Journal of Structural Geology*, v. 12, p. 869-882.

Martel, S. J., 1997. Effects of cohesive zones on small faults and implications for secondary fracturing and fault trace geometry. *Journal of Structural Geology*, v. 19(6), p. 835-847.

Martel, S. J. and Boger, W. A., 1998. Geometry and mechanics of secondary fracturing around small three-dimensional faults in granitic rock. *Journal of Geophysical Research*, v. 103(B9), p. 21,299-21,314.

Martel, S. J., and Pollard, D. D., 1989. Mechanics of slip and fracture along fault zones in granitic rock, Mount Abbot quadrangle, Sierra Nevada, California. *Journal of Geophysical Research*, v. 94, p. 9417-9428.

Martel, S. J., Pollard, D. D., and Segall, P., 1988. Development of simple fault zones in granitic rock, Mount Abbot quadrangle, Sierra Nevada, California. *Geological Society of America Bulletin*, v.100, p. 1451-1465.

Matthäi, S. K. and Belayneh, M., 2004. Fluid flow partitioning between fractures and a permeable rock matrix. *Geophysical Research Letters*, v. 31, L0762, doi: 10.1029/2003GL019027.

Mazurek, M., Bossart, P., and Eliasson, T., 1996. Classification and characterisation of water-conducting fractures at Äspö: Results of observations on the outcrop scale. SKB International Cooperation Report ICR 97-01, Swedish Nuclear Fuel and Waste Management Co., Stockholm.

Mazurek, M., Jakob, A. and Bossart, P., 2003. Solute transport in granitic rocks at Äspö – I: Geologic basis and model calibration. *Journal of Contaminant Hydrology*, v.61, p. 157-174.

McCombie, C. Nuclear waste management worldwide. *Physics Today*, v. 50(6), p. 56-62, 1997.

McKenna, S. A., Meigs, L. C., and Haggerty, R., 2001. Tracer tests in a fractured dolomite: 3. Double-porosity, multiple-rate mass transfer processes in convergent flow tracer tests. *Water Resources Research*, v. 37(5), p. 1143-1154.

Menendez, B., Zhu, W. and Fong, T.-F., 1996. Micromechanics of brittle faulting and cataclastic flow in Berea sandstone. *Journal of Structural Geology*, v. 18(1), p.1-16.

Miller, I., Lee, G., and Sharp, G., 1994. MAFIC matrix/fracture interaction code with solute transport -- User documentation. GAI report, Golder Associates, Redmond, Washington.

Min, K.-B., 2004. Fractured rock masses as equivalent continua – a numerical study. Doctoral thesis, Department of Land and Water Resources Engineering, Swedish Royal Technical Institute.

Moody, J. D. and Hill, M. J., 1956. Wrench-fault tectonics. Geological Society of America Bulletin, v. 67, p. 1207-1246.

Moreno, L. and Neretnieks, I., 1991. Fluid and solute transport in a network of channels. SKB Technical Report 91-44, Swedish Nuclear Fuel and Waste Management Co., Stockholm.

Moreno, L. and Neretnieks, I., 1993. Fluid and solute transport in a network of channels, *Journal of Contaminant Hydrology*, v. 14, p. 163-192.

Moreno, L., Tsang, Y., Tsang, C. F. and Neretnieks, I., 1988. Flow and transport in a single fracture. A two-dimensional statistical model, SKB Technical Report 88-03, Swedish Nuclear Fuel and Waste Management Co., Stockholm.

Morgan, J. K., 1999. Numerical simulations of granular shear zones using the distinct element method. 2. Effects of particle size distribution and interparticle friction on mechanical behavior, *Journal of Geophysical Research*, v. 104(B2), p. 2721-2732.

Morgan, J. K., and Boettcher, M. S., 1999. Numerical simulations of granular shear zones using the distinct element method. 1. Shear zone kinematics and the micromechanics of localization. *Journal of Geophysical Research*, v.104(B2), p. 2703-2719.

Morrow, C. A. and Byerlee, J. D., 1989. Experimental studies of compaction and dilatancy during frictional sliding on faults containing gouge. *Journal of Structural Geology*, v. 11, p. 815-825.

Morrow, C. A., Shi, L. Q., and Byerlee, J. D., 1981. Permeability and strength of San Andreas fault gouge under high pressures. *Geophysical Research Letters*, v. 8(4), p. 325-328.

Morrow, C. A., Shi, L. Q., and Byerlee, J. D., 1984. Permeability of fault gouge under confining pressure and shear stress. *Journal of Geophysical Research*, v 89(B5), p 3193-3200.

Myers, R., and Aydin, A., 1997. The permeability structure of fault zones formed from shearing of preexisting joint zones. *GSA Abstracts with Programs*, p. A-416.

Neretnieks, I., 1980. Diffusion in the rock matrix: An important factor in radionuclide transport? *Journal of Geophysical Research*, v. 85(B8), p. 4379-4397.

Neretnieks, I., Eriksen, T. and Tähtinen, P., 1982. Tracer movement in a single fracture in granitic rock: Some experimental results and their interpretation, *Water Resources Research*, v. 18, p. 849-858.

Neretnieks, I., and Rasmuson, A., 1984. An approach to modelling radionuclide migration in a medium with strongly varying velocity and block sizes along the flow path. *Water Resources Research*, v. 20(12), p.1823-1836.

Neuzil, C. E. and Tracy, J. V., 1981. Flow through fractures, *Water Resources Research*, v. 17, p. 191-199.

Nordenskjöld, C. E., 1944. *Morfologiska studier inom övergångsområdet mellan Kalmarslätt och Tjust* (Morphological studies in the passage area between Kalmar light and Tjust), Carl Bloms Boktryckeri, Lund, 216 p.

Nordqvist, A. W., Tsang, Y. W., Tsang, C.-F., Dverstorp, B., and Andersson, J., 1992. A variable aperture fracture network model for flow and transport in fractured rocks. *Water Resources Research*, v. 28, No. 6, p. 1703-1713.

Novakowski, K. S., Evans, G. V., Lever, D. A. and Raven, K. G., 1985. A field example of measuring hydrodynamic dispersion in a single fracture, *Water Resources Research*, v. 21, No. 8, p. 1165-1174.

Odling, N., 1997. Scaling and connectivity of joint systems in sandstones from western Norway, *Journal of Structural Geology*, v. 19, p. 1257-1271.

Odling, N., 2001. The scaling of hydraulic conductivity in fracture zones. *Geophysical Research Letters*, v. 28(15), p. 3019-3022.

Ohlsson, Y. and Neretnieks, I., 1995. Diffusion data in granite - recommended values, SKB Technical Report TR-95-12, Swedish Nuclear Fuel and Waste Management Co., Stockholm.

Olson, J. E. and Pollard, D. D., 1991. The initiation and growth of en-echelon veins. *Journal of Structural Geology*, v.13, p. 595-608.

Olsson, O. (ed.), 1992. Site characterization and validation – Final report. Stripa Project Technical Report 92-22, Swedish Nuclear Fuel and Waste Management Co., Stockholm.

Osnes, J. D., Winberg, A., and Andersson, J., 1988. Analysis of well test data – Application of probabilistic models to infer hydraulic properties of fractures. Topical Report RSI-0338, RE/SPEC Inc., Rapid City, South Dakota.

Park, S. K. and Roberts, J. J., 2003. Conductivity structure of the San Andreas Fault, Parkfield, revisited. *Geophysical Research Letters*, v. 30(16), p. 1842, doi:10.1029/2003GL017689.

Park, Y. J., and Lee, K. K., 1999. Analytical solutions for solute transfer characteristics at continuous fracture junctions, *Water Resources Research*, v. 35(5), p. 1531-1537.

Park, Y. J., Lee, K. K., and Berkowitz, B., 2001. Effects of junction transfer characteristics on solute in fracture networks. *Water Resources Research*, v. 37(4), p. 909-923.

Peng, S. and Johnson, A. M., 1972. Crack growth and faulting in cylindrical specimens of Chelmsford granite. *International Journal of Rock Mechanics and Mining Science*, v. 9, p. 37-86.

Philip, J., 1988. The fluid mechanics of fracture and other junctions. *Water Resources Research*, v. 24(2), p. 239-246.

Piggott, A. R. and Elsworth, D., 1990. Laboratory studies of transport within a single rock fracture, *Rock Joints: Proceedings of the International Symposium on Rock Joints*, Loen, Norway, June 4-6.

Piper, J. D. A., 1987. *Palaeomagnetism and the Continental Crust*. Open University Press, Milton Keynes, UK.

Poteri, A., Billaux, D., Dershowitz, W., Gómez-Hernandez, J., Cvetkovic, V., Hautojärvi, A., Holton, D., Medina, A., and Winberg, A., 2002. Final report of the TRUE Block Scale project: 3. Modelling of flow and transport. SKB Technical Report TR-02-15, Swedish Nuclear Fuel and Waste Management Co., Stockholm.

Påsse, T., 2001. An empirical model of glacio-isostatic movements and shore-level displacement in Fennoscandia. SKB Report R-01-41, Swedish Nuclear Power and Fuel Co., Stockholm.

Prabhu, N. U., 1965. *Stochastic Processes: Basic Theory and Its Applications.* MacMillan Co., New York, 233 p.

Pyrak-Nolte, L. J., Myer, L. R. and Cook, N. G. W. 1985. Determination of fracture void geometry and contact area as a function of applied load, in *Earth Sciences Division Annual Report 1985*, report LBL-20450, Lawrence Berkeley Laboratory, Berkeley, California, p. 16-17.

Pyrak-Nolte, L. J., Cook, N. G. W. and Nolte, D. D., 1988. Fluid percolation through single fractures, *Geophysical Research Letters*, v. 15, p. 1247-1250.

Press, W. H., Flannery, B. P., Teukolsky, S. A., and Vetterling, W. T., 1986. *Numerical Recipes: The Art of Scientific Computing*, Cambridge University Press, Cambridge, 818 p.

Raven, K. G., Novakowski, K. S., and Lapcevic, P. A., 1988. Interpretation of field tracer tests in a single fracture using a transient solute storage model, *Water Resources Research*, v. 24, p. 2019-2032.

Renshaw, C. E., 2000. Fracture spatial density and the anisotropic connectivity of fracture networks. In Faybishenko, B., Witherspoon, P.A., and Bencon, S.M., *Dynamics of Fluids in Fractured Rock, Geophysical Monograph 122*, American Geophysical Union, Washington, D.C.

Renshaw, C.E. and Pollard, D.D., 1994. Numerical simulation of fracture set formation: A fracture mechanics model consistent with experimental observations. *Journal of Geophysical Research*, v. 99, p. 9359-9372.

Robeson, K. R. and Evans, J. P., 1997. Three-dimensional structure of a small strike slip fault zone, *Abstracts with Programs - Geological Society of America*, v. 29(6), p. 258.

Robinson, P. C., 1984. Connectivity, flow and transport in network models of fractured media. Ph. D. dissertation, St. Catherine's College, Oxford University, Oxford, England.

Robinson, J. W., and Gale, J. E., 1990. A laboratory and numerical investigation of solute transport in discontinuous fracture systems, *Ground Water*, v. 28(1), p. 25-36.

Roux, S., Plouraboue, F., and Hulin, J. P., 1998. Tracer dispersion in rough open cracks, *Transp Porous Media*, v. 32, p. 97-116.

Rudberg, S., 1954. Västerbottens berggrundmorfologi, ett för till rekonstruktions av preglaciala erosionsgenerationer I Sverige. *Geografiska skifter från Upsala Universitets Geografiska Institution*, Appelbergs Boktryckeri AB, Uppsala, 457 p.

Sahimi, M., 1995. *Flow and Transport in Porous Media and Fractured Rock: From classical methods to modern approaches*. VCH, Weinheim, Germany, 482 p..

Schrauf, T. W. and Evans, D. D., 1986. Laboratory studies of gas flow through a single fracture, *Water Resources Research*, v. 22, p. 1038-1050.

Schulson, E. M., Biescu, D., and Renshaw, C. E., 1999. On the initiation of shear faults during compressive brittle failure: A new mechanism. *Journal of Geophysical Research*, v. 104(B1), p. 695-705.

Schulz, S. E. and Evans, J. P., 1998. Spatial variability in microscopic deformation and composition of the Punchbowl Fault, southern California: implications for mechanisms, fluid-rock interaction and fault morphology. *Tectonophysics*, v. 295, p. 223-244.

Schulz, S. E. and Evans, J. P., 2000. Mesoscopic structure of the Punchbowl Fault, southern California and the geological and geophysical structure of active strike-slip faults. *Journal of Structural Geology*, v. 22, p. 913-930.

Segall, P. and Pollard, D. D., 1980. Mechanics of discontinuous faults. *Journal of Geophysical Research*, v. 85, p. 4337-4350.

Segall, P., and Pollard, D. D., 1983. Joint formation in granitic rock of the Sierra Nevada, *Geologic Society of America Bulletin*, v. 94, p. 563-575.

Shapiro, A. M., 1988. Interpretation of Tracer Tests Conducted in an Areally Extensive Fracture in Northeastern Illinois, *Symposium Proceedings of International Conference on Fluid Flow in Fractured Rocks*, Georgia State University, Atlanta, Georgia, May 15-18, p. 12-22.

Shapiro, A. M., and Anderson, J., 1985. Simulation of steady-state flow in three-dimensional networks using the boundary element method. *Advances in Water Resources*, v. 8, p. 106-110.

Sharp, J. C., 1970. Fluid flow through fissured media. Ph. D. dissertation, University of London, Imperial College of Science and Technology, London, U.K.

Sibson, R. H., 1973. Interactions between temperature and pore pressure during earthquake faulting. *Nature*, v. 243, p. 66-68.

Sibson, R. H., 1977. Fault rocks and fault mechanisms. *Geological Society of London Journal*, v. 133, p. 191-231.

Sibson, R. H. 1981. Controls on low-stress hydro-fracture dilatancy in thrust, wrench, and normal fault terrains. *Nature*, v. 289, p. 665-667.

Sibson, R. H., 1992. Implications of fault-valve behavior for rupture nucleation and recurrence. *Tectonophysics*, v. 221, p. 283-293.

Sibson, R. H., 1996. Structural permeability of fluid-driven fault-fracture meshes. *Journal of Structural Geology*, 18(8), p. 1031-1042.

SKB, 1999. SR-97 – Post-closure safety assessment. SKB Technical Report 99-06, Swedish Nuclear Fuel and Waste Management Co., Stockholm.

SKB, 2004. Preliminary site description: Simpevarp area – Version 1.1. SKB Report R-04-25, Swedish Nuclear Fuel and Waste Management Co., Stockholm.

Smith, L., Forster, C. B., and Evans, J. P., 1989. Interaction of fault zones, fluid flow, and heat transfer at the basin scale. In Neuman, S. P. and Neretnieks, I., eds., *Hydrogeology of Low Permeability Environments*. International Association of Hydrogeologists, v. 2, p. 41-67. Verlag Heinz Heise, Hannover, Germany.

Snow, D. T., 1969. Anisotropic permeability of fractured media. *Water Resources Research* 5(6):1273-1289.

Stephens, M. B., 1988. The Scandinavian Caledonides: A complexity of collisions. *Geology Today*, Jan-Feb 1988, p. 20-25.

Stephansson, O., Ljunggren, C., and Jing, L., 1991. Stress measurements and tectonic implication for Scandinavia. *Tectonophysics*, v. 189, p. 317-322.

Stockman, H. W., Li, C., and Wilson, J. L., 1997. A lattice-gas simulation and lattice-Boltzmann study of mixing at continuous fracture junctions: Importance of boundary conditions. *Geophysical Research Letters*, v. 24(12), p. 1515-1518.

Stanfors, R., Erlström, M. and Markström, I, 1991.. Äspö Hard Rock Laboratory: Overview of the investigations 1986-1990. SKB Technical Report 91-20, Swedish Nuclear Fuel and Waste Management Co., Stockholm.

Stratford, R. G., Herbert, A. W. and Jackson, C. P., 1990. A parameter study of the influence of aperture variation on fracture flow and the consequences in a fracture network, *Rock Joints: Proceedings of the International Symposium on Rock Joints*, Loen, Norway, June 4-6, p. 413-422.

Sudicky, E. A., 1989. The Laplace transform Galerkin technique: A time-continuous finite element theory and application to mass transport in groundwater. *Water Resources Research*, v. 25(8), p. 1833-1846.

Sudicky, E. A. and Frind, E. G. 1982. Contaminant transport in fractured porous media: Analytical solutions for a system of parallel fractures, *Water Resources Research*, v. 18(6), p. 1634-1642.

Sudicky, E.A. and McLaren, R.G., 1992. The Laplace transform Galerkin technique for large scale simulation of mass transport in discretely fractured porous formations. *Water Resources Research*, v. 28(2), p. 499-514.

Sultan, L., Claesson, S., Plink-Björklund, P., and Björklund, P., 2004. Proterozoic and Archaean detrital zircon ages from the Palaeoproterozoic Västervik Basin, southern Fennoscandian Shield. *Geologiska Föreningens I Stockholm Förhandlingar*, v.126, p. 39.

Switek, D. P., 1994. Faults as potential hydrocarbon barriers, Arroyo Grande, California. M.S. Thesis, Texas A & M University.

Talbot, C. J., and Munier, R., 1989. Faults and fracture zones on Äspö. SKB Swedish Hard Rock Laboratory Progress Report 25-89-11, Swedish Nuclear Fuel and Waste Management Co., Stockholm.

Taylor, G. I., 1953. Dispersion of soluble matter in solvent flowing slowly through a tube. *Proceedings of the Royal Society of London A*, v. 219, p. 186-203.

Tirén, S., 1989. Geological setting and deformation history of a low angle fracture zone at Finnsjön, Sweden, in SKB Technical Report 89-19, Swedish Nuclear Fuel and Waste Management Co., Stockholm.

Tirén, S., and Beckholmen, M., 1990. Rock block configuration in Southern Sweden and crustal deformation. *Geologiska Föreningens I Stockholm Förhandlingar*, v. 112(4), p. 361-364.

Tirén, S.A., Askling, P., and Wänstedt, S., 1999. Geologic site characterization for deep nuclear waste disposal in fractured bedrock based on 3D data visualization, *Engineering Geology*, v. 52, p. 319-346.

Tirén, S.A., Beckholmen, M., Voss, C., and Askling, P., 1996. Development of a geological and structural model of Äspö, southeastern Sweden (SITE-94), SKI Report 96:16, Swedish Nuclear Power Inspectorate, Stockholm.

Tirén, S.A., Wedholm, K., Sträng, T., and Geier, J., 2005. Field study of fracture zones exposed in two adjacent roadcuts in granitic rock. Comparison with interpreted lineaments and characterisation of internal structural variability. Ekolsund/Grillby area, Uppland, south-central Sweden. SKI Report R 05-xx [in preparation], Swedish Nuclear Power Inspectorate, Stockholm.

Tsang, C. F. and Doughty, C., 2003. A particle-tracking approach to simulating transport in a complex fracture. *Water Resources Research*, v. 37(7),1174, doi: 10.1029/2002WR001614.

Tsang, Y. W., 1984. The effects of tortuosity on fluid flow through a single fracture, *Water Resources Research,* v. 20, p. 1209-1215.

Tsang, Y. W. and C. F. Tsang, 1987. Channel model of flow through fractured media, *Water Resources Research,* v. 23, p. 467-479.

Tsang, Y. W. and Tsang, C. F., 2001. A particle-tracking method for advective transport in fractures with diffusion into finite matrix blocks. *Water Resources Research*, v. 37(3), p. 831-835.

Tsang, Y.W., Tsang, C. F., Hale, F. V., and Dverstorp, B., 1996. Tracer transport in a stochastic continuum model of fractured media, *Water Resources Research*, v. 32(10), p. 3077-3092.

Tsang, Y.W. and Witherspoon, P.A., 1981. Hydromechanical behavior of a deformable rock fracture subject to normal stress, *Journal of Geophysical Research,* v. 86, p. 9287-9298.

Tsang, Y.W. and Witherspoon, P.A., 1983. The dependence of fracture mechanical and fluid flow properties on fracture roughness and sample size, *Journal of Geophysical Research,* v. 88, p. 2359-2366.

Tullborg, E.-L., Larsson, S.-Å., and Stiberg, J.-P., 1996. Subsidence and uplift of the present land surface in the southeastern part of the Fennoscandian Shield. *Geologiska Föreningens I Stockholm Förhandlingar*, v. 118, p. 126-128.

Turcotte, D.L., 1986. Fractals and fragmentation. *Journal of Geophysical Research*, v. 91(B2), p. 1921-1926.

Voss, C., Tirén, S., and Glynn, P., 1996. Hydrogeology of Äspö Island, Simpevarp, Sweden (SITE-94), SKI Report 96:13, Swedish Nuclear Power Inspectorate, Stockholm.

Valkiainen, M., Aalto, H., Lehikoinen, J., and Uusheimo, K., 1996. The effect of thickness in the through-diffusion experiment. Technical Research Centre of Finland (VTT), Espoo, Finland, 33 p.

Waite, M. E., Ge, S., Spetzler, H. and Bahr, D.B., 1998. The effect of surface geometry on fracture permeability: A case study using a sinusoidal fracture, *Geophysical Research Letters*, v. 25(6), p. 813-816.

Wahlgren, C.-H., Persson, I., Danielsson, P. Berglund, J., Triumf, C.-A., Mattsson, H., and Thunehed, H., 2003. Geologiskt underlag för val av prioriterad plats inom området väster om Simpevarp, Delrapport 1-4, SKB P-03-06, Swedish Nuclear Fuel and Waste Management Co., Stockholm.

Wallace, R. E., 1973. Surface fracture patterns along the San Andreas fault, *in* Kovach, R.L. and Nur, A., eds., *Proceedings of the Conference on Tectonic Problems of the San Andreas Fault System*, Stanford University Publication Geological Science, v. XIII, p. 173-180.

Wang, J. S. Y. and Narasimhan, T. N., 1988. Fractal and statistical characterization of rough fracture, *Symposium Proceedings of International Conference on Fluid Flow in Fractured Rocks*, Georgia State University, Atlanta, Georgia, May 15-18, p. 220-228.

Wang, J. S. Y, Narasimhan, T. N. and Scholz, C.H., 1988. Aperture correlation of a fractal fracture, *Journal of Geophysical Research*, v. 93, p. 2216-2224.

Warren, T. E. and Root, P. J., 1963. The behavior of naturally fractured reservoirs, *Society of Petroleum Engineers Journal*, v. 3, p. 245-255.

Willemse, E. J. M., and Pollard, D. D., 1998. On the orientation and patterns of wing cracks and solution surfaces at crack tips. *Journal of Geophysical Research*, v. 103(B2), p. 2427-2438.

Wilson, C. R., 1970. An investigation of laminar flow in fractured porous rocks. Ph.D. thesis, University of California, Berkeley, 178 p.

Winberg, A., Andersson, P., Poteri, A., Cvetkovic, V., Dershowitz, W., Hermanson, J., Gómez-Hernandez, J., Hautojärvi, A., Billaux, D., Tullborg, E.-L., Holton, D., Meier, P., and Medina, A., 2002. Final report of the TRUE Block Scale project: 4. Synthesis and retention in the block scale. SKB Technical Report TR-02-16, Swedish Nuclear Power and Fuel Co., Stockholm.

Witherspoon, P.A., 1979. Observations of a potential size effect in experimental determination of the hydraulic properties of fractures, *Water Resources Research*, v. 15, p. 1142-1146.

Witherspoon, P. A., Wang, J. S. Y., Iwai, K. and Gale, J. E., 1979. Validity of cubic law for fluid flow in a deformable rock fracture, Report LBL-9557/SAC-23/UC-70, Swedish-American Cooperative Program on Radioactive Waste Storage in Mined Caverns in Granitic Rock, Swedish Nuclear Fuel and Waste Management Co., Stockholm.

Witherspoon, P. A., Wang, J. S. Y., Iwai, K. and Gale, J. E., 1980. Validity of cubic law for fluid flow in a deformable rock fracture, *Water Resources Research*, v. 16, p. 1016-1024.

Wörman, A., Geier, J., and Xu, S., 2004. Modelling of radionuclide transport by groundwater motion in fractured bedrock for performance assessment purposes. SKI Report 2004:14, Swedish Nuclear Power Inspectorate, Stockholm.

Xu, S., Wörman, A., and Dverstorp, B., 2001. Heterogeneous matrix diffusion in crystalline rock – implications for geosphere retardation of migrating radionuclides. *Journal of Contaminant Hydrology*, v. 47(2-4), p. 365-378.

Yeo, I. W. and Ge, S., 2001. Solute dispersion in rock fractures by non-Darcian flow, *Geophysical Research Letters*, v. 28(20), p. 3983-3986.

Zhang, X. and Sanderson, D.J., 1996. Numerical modelling of the effects of fault slip on fluid flow around extensional faults. *Journal of Structural Geology*, v. 18(1), p. 109-119.

Zimmerman, R. W., Chen, D. W., Long, J. C. S. and Cook, N. G. W., 1990. Hydromechanical coupling between stress, stiffness, and hydraulic permeability of rock joints and fractures, *Rock Joints: Proceedings of the International Symposium on Rock Joints*, Loen, Norway, June 4-6, p. 571-577.

Zimmerman R.W. and Bodvarsson, G.S., 1996. Hydraulic conductivity of rock fractures, *Transp. Porous Media*, v. 23, p. 1-30.

Zimmerman R. W., Kumar, S., and Bodvarsson, G. S., 1991. Lubrication theory analysis of the permeability of rough-walled fractures, *Int. J. Rock Mech. Min Sci. Abstr.*, v. 28, p. 325-331.

Zoback, M. D., Zoback, M. L., Mount, V., Eaton, J., Healy, J., Oppenheimer, D., Reasonberg, P., Jones, L., Raleigh, B., Wong, I., Scotti, O., and Wentworth, C., 1987. New evidence on the state of stress of the San Andreas fault system. *Science*, v. 238, p. 1105-1111.

APPENDICES

Appendix A Preparation of detailed maps of fracture zones

The detailed-scale mapping of the fracture zones at Äspö was carried out in May, 1999 as follows. A reference line was laid on the outcrop by compass sighting. A 1 m x 1 m square frame, with 10 cm x 10 cm grid divisions, was laid over the rock in alignment with the reference line, and moved along the reference line in overlapping increments. For each frame position, the inclination of the frame was measured along two orthogonal sides, and the rock surface was photographed from a height of about 2.5 m using a step ladder. To produce a 1:10 scale field map of the N to NNW trending zone, the fracture configuration for each frame position was sketched on 2 mm graph paper by scaling fracture traces from the 10 cm x 10 cm grid to 1 cm x 1 cm squares on the paper.

In this way a continuous photographic mosaic was produced, within which the true coordinates of points along fractures could be determined by comparison to the reference grid. The outcrops were also filmed with a hand-held video camera, to provide a continuous record of each outcrop. Photographs from this work have been stored both as the original film (slides and print negatives, giving maximum resolution) and as scanned, high-resolution digital images in JPEG format on CD-ROMs for computer analysis.

As a check on the photographic mapping method, a 1:10 scale field map was prepared for a 1 m x 6 m portion of one N-striking zone, by sketching directly from the outcrop. The fracture configuration was sketched on 2 mm graph paper by scaling fracture traces from the 10 cm x 10 cm grid to 1 cm x 1 cm squares on the paper. Fracture strikes and dips were measured on the outcrop for 48 of the most extensive fractures on this map.

Working with the digital images, the fracture traces were digitized as graphical overlays on the computer screen. Correction for photographic distortion was made by use of a digital rubber-sheeting algorithm in the *splinter* analysis program (on accompanying CD-ROM), to transform the digitized traces and grid lines so that the quadrilaterals formed by intersecting grid lines throughout the image are restored to 10 cm squares.

At the Ekolsund site, the photographic mapping procedure was modified as the 1 m square grid was not practical for use on the near-vertical, larger-scale exposures. Instead, reference points were marked on the rock face with spray paint (water-soluble so that the rock would not be permanently defaced) prior to photographing the outcrops with a digital camera. Distances between pairs of reference points were measured by tape, to allow construction of a

Euclidean distance matrix which could be used to correct for photographic distortion and large-scale nonplanarity of the exposures.

The method for mapping individual traces was also modified to allow better checking of fracture traces in the field. The digital images were printed onto A4 (30 cm x 21 cm) paper and laminated, to provide a base for sketching fracture traces at an approximately 1:10 scale, directly on the printed images, while viewing the exposure.

For the detailed mapping of fracture zones, the aim was to identify and sketch all fractures and faults longer than 10 cm, within the entire area covered by the photograph. Structural details including splays and fragmented or brecciated zones within small faults were mapped in this way to an estimated resolution of about 2 cm. Fracture orientations and directions of lineations and slickensides were measured for the larger fractures and noted on the field map.

Finally each field map (laminated image with sketched fracture traces) was scanned so that the fracture traces could be digitized and analyzed, by the same procedures used for the Äspö images. With the procedure adopted at Ekolsund, the digitization was simplified, and reliability improved, by identifying and verifying each fracture trace at the exposure, rather than only from a digital image of limited resolution.

The graphical map analysis program *splinter* (included as supplementary digital materials), was used to calculate the coordinates of the digitized fracture traces in an orthogonal coordinate system aligned with geographic north, and to correct for skewed photographic angles, lens distortion (convergence) and tilt of the reference frame. After converting the digitized fracture traces to real-world coordinates, the traces from each image were combined to produce a single map of each exposure. As a final step, the reference grid lines were removed to give a clean map.

The end product, for each exposure, is a single map that show fracture traces on scales from a few mm up to over 10 m. Thus the maps show structural details on scales that range over four orders of magnitude.

The initial digitization from photographic images was done with a commercial, computer-assisted drawing software which allowed zooming to arbitrarily fine scales and drawing of vector-format lines over a digital image. The fracture trace and grid coordinates, as digitized from the images, were stored in AutoCAD (DXF) vector format for further processing and analysis using the program *splinter*. This is an interactive, graphical code

based on the *gtk* free-software toolkit, which is supported on the Linux platform. The *splinter* code was developed as part of this research program, and included on the accompanying CD-ROM.

Corrections for skewed photographic angle, camera lens distortion, and frame tilt were made by marking "pinpoints" of known coordinates on plots of the fracture traces and reference grid lines,. Given the known coordinates of these points, and frame tilt data as measured in the field, *splinter* calculates a rotation matrix and x-y polynomial of appropriate order, to map the plotted points into the real-world coordinate system. The order of the polynomial is increased when more points are specified, to allow smooth, spatially variable transformations ("rubber-sheeting") which map each pinpoint to the exact, specified coordinates, while intervening areas of the plot may be mapped nonlinearly, *e.g.* to correct for photographic distortion.

This method does not correct for all sources of error in the photographic mapping process. Nonplanarity of the outcrop surface, in combination skewed photographic angles and lens distortion, can result in errors in the mapped positions of points, even after making the corrections described above. Such errors are minimized, but not eliminated, by photographing from an angle that is close to perpendicular to the plane of the reference frame and outcrop surface.

Comparison of corresponding points from overlapping pairs of images indicates that the magnitude of such errors is typically less than 5 mm between adjacent, 1 m square frame positions. Typical manual errors in digitization, which affect comparisons between fractures that are adjacent to each other on a single image, are estimated to be 1 mm or less.

A complete map of the outcrop was assembled by combining the trace data from adjacent, photographed panels. Small offsets between adjacent map panels, due to errors such as described above, were corrected by applying a uniform linear displacement to bring the corresponding points into alignment. The residual errors between points that could not be brought into agreement in this manner were typically 3 mm or less.

Appendix B Discrete Feature Model for flow and solute transport in fractured granitic rock

A discrete-feature modeling (DFM) code for numerical simulation of flow and transport in a network of discrete features was developed as one part of this research. The code is based on the finite-element method, and is designed for the following general conceptualization of the hydrogeological system in the bedrock.

Features are planar or piecewise-planar entities representing fractures, fracture zones, disturbed zones around tunnels, or other water-conducting elements in the rock. The geometry of the features is defined in terms of triangular elements with connections defined by nodes (vertices) that are shared between elements.

Boundaries are defined in terms of groups of element vertices which are in contact with a specific physical boundary or segment of a boundary, such as a section of a borehole, a tunnel, or the ground surface. Boundary conditions are assigned to these boundary groups for each stage of the simulation.

Fluid flow simulations are restricted to the case of a single-phase, uniform-density, Newtonian fluid, *e.g.* groundwater under conditions of complete saturation and negligible density variation.

Steady-state flow is modeled by the Galerkin finite-element method. Transient flow may be modeled either by a backward-difference scheme, or by a Laplace-transform Galerkin (LTG) formulation of the finite-element equations. In a given stage of a flow simulation, the boundary conditions at a given boundary group may be specified head, specified flux, or specified net flux.

Transport simulations are restricted to the case of a single dissolved species at dilute concentrations (*i.e.* low enough to neglect the influence of concentration on fluid density gradients), influenced by advection and diffusion (including dispersion phenomena), sorption, and matrix diffusion.

Transport is modeled either by a discrete-parcel random-walk (particle-tracking) method or by a LTG formulation of the finite-element equations for advection and dispersion. Two alternative particle-tracking algorithms are supported: 2-D advective-dispersive transport within a given element, or 3-D advective-diffusive transport with an assumed parabolic velocity profile giving rise to Taylor dispersion. In a given stage of a transport simulation, the

boundary conditions at a given boundary group may be specified concentration, specified mass flux, or specified net mass flux.

As in an ordinary 2-D, finite-element mesh, the geometry of the mesh is encoded as an ordered list of global coordinate vectors $\{\boldsymbol{x}_n, n = 1, 2, ..., N_n\}$ for each of the N_n unique nodes (element vertices) in the mesh, and as a list of N_e triangular elements, each of which is defined by a triplet of node indices $\{n_{e1}, n_{e2}, n_{e3}\}$ and by a vector of parameter values $\{S_e, T_e, b_e, ...\}$ which are derived from the parent feature of the element. The mesh differs from an ordinary 2-D mesh in that the global coordinates $\boldsymbol{x}_n$ are necessarily specified in 3-D, and in that element nodes and edges that lie along intersections between two or more different features are shared among the elements formed from the different features, to account for the hydrologic connections between features.

Four different types of boundary conditions (BCs) are employed:

Type 1: Specified head:

$$h_n(t) = \hat{h}_B(\boldsymbol{x},t)\big|_{\boldsymbol{x}=\boldsymbol{x}_n}, \qquad n \in B$$

Type 2: Specified flux:

$$Q_n(t) = \int_{A_B} \hat{q}_B(\boldsymbol{x},t)\,\psi_{B,n}(\boldsymbol{x})\,dA, \qquad n \in B$$

Type 3: Specified net flux:

$$\sum_{n \in B}^{N} Q_n(t) = \hat{Q}_B(t); \qquad h_{bn}(t) = h_B(t), \quad n \in B$$

Type 4: Specified infiltration per unit surface area:

$$Q_n(tQ_n(t)) = \sum_{e:n\subset \boldsymbol{n}_e} \int_e \hat{q}_B(\boldsymbol{x},t)\,\psi_e(\boldsymbol{x})\,dA, \quad n \in B$$

where circumflexes denote specified (*i.e.* known) quantities, and where Q_n and h_n are the flux

(into the mesh) and head at a given node, $Q_B(t)$ is the specified influx (m^3/s) and h_B is the head at a given boundary B, and $\psi_{e(n)}$ is the element basis function associated with the eth element at node n.

The specified-net-flux BC is used to account for the "superconductive" connection that occurs where several features are intersected by a given borehole section. For passive monitoring sections, Q_B is set to zero, and for actively pumped sections, Q_B is set to the specified pumping rate.

Simulation sequences of arbitrary complexity can be constructed as a series of stages, within each of which flow and/or transport is simulated with respect to a specified set of boundary conditions. The results of each stage serving as the initial conditions for the next stage.

Simulation sequences are defined in input files that specify the mesh to be used, and for each stage, the boundary conditions, physical parameters, and solver options. Plain-text, free-format input based on keyword recognition (rather than order of input) is supported for straightforward checking and documentation of simulations. Boundaries can be referenced by site-specific names (*e.g.* "Borehole_KAS07" or "ground_surface"). Physical parameters can be specified in terms of units used in the field data; the code automatically checks for correct dimensionality and scales the numerical values to SI units for internal calculations.

Development and documentation of the code is ongoing in relation to other projects. A copy of the version of the source code used for this research, and current draft user documentation, are included in supplemental electronic materials with this dissertation. The code is written in standard ANSI C but has only been tested on a Linux platform using the GNU compiler.

The following sections give mathematical details of the flow and solute transport solvers.

Derivation of matrix equations for flow

At a given point $\boldsymbol{x}$ in a medium with transmissivity $T(\boldsymbol{x})$ and storativity $S(\boldsymbol{x})$, conservation of mass combined with Darcy's law yields the transient flow equation:

$$S\frac{\partial h}{\partial t} \;=\; \nabla\cdot(T\nabla h) \;+\; q_i\delta(\boldsymbol{x}-\boldsymbol{x}_i) \;=\; S\frac{\partial h}{\partial t}$$

where h is hydraulic head, t is time, and q_i is the influx (water entering the medium) from a point source at $\boldsymbol{x}_i$.

Let:

$$\hat{h}(\boldsymbol{x},t) \;=\; \sum_{j=1}^{N} h_j(t)w_j(\boldsymbol{x})$$

be a discrete approximation of $h(\boldsymbol{x},t)$, where $h_j(t)$ is the hydraulic head at the jth node, j = 1, 2, ... , N, and where $w_j(\boldsymbol{x})$ is some spatial weighting function. Substituting for h in (1) we obtain:

$$S\sum_{j=1}^{N}\frac{\partial h_j}{\partial t}w_j \;-\; \nabla\cdot\left(T\sum_{j=1}^{N}h_j\nabla w_j\right) \;+\; q_i\delta(\boldsymbol{x}-\boldsymbol{x}_i) \;=\; -\,S\sum_{j=1}^{N}\frac{\partial h_j}{\partial t}w_j 0$$

or:

$$\sum_{j=1}^{N}\nabla\cdot(T\nabla w_j)h_j \;-\; \sum_{j=1}^{N}Sw_j\frac{dh_j}{dt} \;+\; q_i\delta(\boldsymbol{x}-\boldsymbol{x}_i) \;=\; 0$$

Requiring orthogonality with respect to the weighting functions, and choosing weighting functions that are defined piecewise on individual element areas A^e, so that $w_i = 0$ for $\boldsymbol{x}_i \notin A^e$, gives:

$$0 = \int_A \left\{ \sum_{j=1}^{N} h_j \nabla \cdot (T \nabla w_j) - \sum_{j=1}^{N} \frac{dh_j}{dt} S w_j + q_i \delta (\boldsymbol{x} - \boldsymbol{x}_i) \right\} w_i dA$$

$$= \sum_{j=1}^{N} \left[h_j \sum_e \int_{A^e} w_i \nabla \cdot (T \nabla w_j) dA - \frac{dh_j}{dt} \sum_e \int_{A^e} w_i S w_j dA \right] + \sum_e \int_{A^e} q_i \delta (\boldsymbol{x} - \boldsymbol{x}_i) w_i dA$$

where the summation over e is understood to indicate summation over all elements e.

If node locations are chosen such that any source/sink term q_i coincides with a node at $\boldsymbol{x}_i$, then:

$$\sum_e \int_{A^e} q_i \delta (\boldsymbol{x} - \boldsymbol{x}_i) w_i dA = q_i$$

since $w_i = 1$ at $\boldsymbol{x}_i$. Defining:

$$d_{ij}^e = \int_{A^e} S w_i w_j dA$$

$$a_{ij}^e = \int_{A^e} w_i \nabla \cdot (T \nabla w_j) dA$$

and defining the NxN matrices $\mathbf{A} = [\sum a^e_{ij}]$ and $\mathbf{D} = [\sum d^e_{ij}]$ and the 1xN column vectors $\boldsymbol{h}(t) = [h_j(t)]^T$ and $\boldsymbol{q}(t) = [q_i(t)]^T$, the preceding equation may be written as:

$$\mathbf{A}\boldsymbol{h}(t) - \mathbf{D}\frac{d\boldsymbol{h}}{dt} = -\boldsymbol{q}(t) + \mathbf{D}\boldsymbol{h}(0)$$

or by rearranging we obain the general matrix equation for transient flow:

$$\mathbf{D}\frac{d\boldsymbol{h}}{dt} - \mathbf{A}\boldsymbol{h}(t) = \boldsymbol{q}(t)$$

Steady-state flow

For steady-state flow, $d\mathbf{h}/dt = 0$ and the finite-element equation is simply:

$$\mathbf{A}\boldsymbol{h}(t_\infty) = -\boldsymbol{q}(t_\infty)$$

Laplace-Galerkin formulation for transient flow

In the following, the Laplace transform with respect to t of a given function $f(t)$ will be denoted by an overbar, *i.e.*:

$$\mathcal{L}[f(t)] = \int_0^\infty f(t)\mathrm{e}^{-st}dt = \bar{f}(s)$$

From the properties of the Laplace transform, $\mathcal{L}[d\mathbf{h}/dt\,] = s\mathcal{L}[\boldsymbol{h}(t)] - \boldsymbol{h}(0)$. Substituting this relationship into the Laplace transform of the general matrix equation for transient flow gives:

$$\mathbf{D}[s\bar{\boldsymbol{h}}(s) - \boldsymbol{h}(0)] - \mathbf{A}\bar{\boldsymbol{h}}(s) = \bar{\boldsymbol{q}}(s)$$

or:

$$[s\mathbf{D} \mp \mathbf{A}]\bar{\boldsymbol{h}}(s) = \bar{\boldsymbol{q}}(s) + \mathbf{D}\boldsymbol{h}(0)$$

Backward-difference formulation for transient flow

The backward-difference approximation of the time derivative is:

$$\left(\frac{d\boldsymbol{h}}{dt}\right)_{t=t_{n+1}} \approx \frac{\boldsymbol{h}(t_{n+1}) - \boldsymbol{h}(t_n)}{t_{n+1} - t_n} = \frac{\boldsymbol{h}_{n+1} - \boldsymbol{h}_n}{\Delta t_{n+1}}$$

Substituting this approximation for the time derivative in the general matrix equation for transient flow:

$$\frac{1}{\Delta t_{n+1}}\mathbf{D}[\boldsymbol{h}_{n+1} - \boldsymbol{h}_n] - \mathbf{A}\boldsymbol{h}_{n+1} = \boldsymbol{q}_{n+1}$$

or:

$$\left[\frac{1}{\Delta t_{n+1}}\mathbf{D}\boldsymbol{h}_{n+1}] - \mathbf{A}\right]\boldsymbol{h}_{n+1} = \boldsymbol{q}_{n+1} + \frac{1}{\Delta t_{n+1}}\mathbf{D}\,\boldsymbol{h}_n$$

which can be solved stepwise for the head vectors $\boldsymbol{h}_i = \boldsymbol{h}(t_i)$, i=1,2, ..., given the initial head vector $\boldsymbol{h}_0 = \boldsymbol{h}(t_0)$.

Finite element coefficients

Case 1: $S(\boldsymbol{x})$ and $T(\boldsymbol{x})$ piecewise constant

If $S(\boldsymbol{x})$ and $T(\boldsymbol{x})$ are constant within each element, *i.e.* $S(\boldsymbol{x}) = S_e$ and $T(\boldsymbol{x}) = T_e$, then $\nabla T = 0$ and:

$$d_{ij}^e = \int_{A^e} S_e w_i w_j dA = S_e \int_{A^e} w_i w_j dA$$

$$\begin{aligned} a_{ij}^e &= \int_{A^e} w_i \nabla (T_e \nabla w_j) dA = T_e \int_{A^e} w_i \nabla^2 w_j dA \\ &= T_e \left[\int_{A^e} \nabla \cdot (w_i \nabla w_j) dA - \int_{A^e} \nabla w_i \cdot \nabla w_j dA \right] \\ &= T_e \left[\int_{\partial A^e} w_i \nabla w_j \cdot \boldsymbol{n}\, ds - \int_{A^e} \nabla w_i \cdot \nabla w_j dA \right] \end{aligned}$$

by Gauss' divergence theorem.

Case 2: $S(\boldsymbol{x})$and $T(\boldsymbol{x})$ piecewise linear

If $S(\boldsymbol{x})$and $T(\boldsymbol{x})$ are taken to be piecewise linear within each element:

$$T(\boldsymbol{x}) = \sum_{k \in e} T_k w_k(\boldsymbol{x}) = \sum_{k \in e} T_k w_k(\boldsymbol{x})$$

$$S(\boldsymbol{x}) = \sum_{k \in e} T_k w_k(\boldsymbol{x}) = \sum_{k \in e} T_k w_k(\boldsymbol{x})$$

then:

$$d_{ij}^{e}\mathbf{D} = \sum_{k\in e} S_k d_{ijk}^{e}, \qquad d_{ijk}^{e} = \int_{A^e} w_i w_j w_k \, dA$$

$$a_{ij}^{e} = \sum_{k\in e} T_k a_{ijk}^{e}, \qquad a_{ijk}^{e} = \int_{A^e} w_i [\nabla\cdot(w_k \nabla w_j)] \, dA$$

By expanding the dot product and making use of the identity $\nabla\cdot(w_i w_k \nabla w_j) = \nabla(w_i w_k)\cdot\nabla w_j + w_i w_k \nabla^2 w_j$, the coefficients a_{ijk} can be expressed as:

$$a_{ijk}^{e} = \int_{A^e} w_i (\nabla w_k \cdot \nabla w_j) \, dA + \int_{A^e} w_i w_k \nabla^2 w_j \, dA$$

$$= \int_{A^e} w_i (\nabla w_k \cdot \nabla w_j) \, dA + \int_{A^e} \nabla\cdot(w_i w_k \nabla w_j) \, dA - \int_{A^e} \nabla(w_i w_k)\cdot\nabla w_j \, dA$$

$$= \int_{\partial A^e} w_i w_k \nabla w_j \cdot \mathbf{n} \, ds - \int_{A^e} (\nabla w_i \cdot \nabla w_j) w_k \, dA$$

Laplace-Galerkin formulation of transient flow problem

At a given point $\boldsymbol{x}$ in a medium with transmissivity $T(\boldsymbol{x})$ and storativity $S(\boldsymbol{x})$, conservation of mass combined with Darcy's law yields the transient flow equation:

$$S\frac{\partial h}{\partial t} = \nabla\cdot(T\nabla h) + q_i\delta(\boldsymbol{x}-\boldsymbol{x}_i)$$

where h is hydraulic head, t is time, and q_i is the influx from a point source at $\boldsymbol{x}_i$.

Taking the Laplace transform with respect to t gives:

$$S(s\bar{h}-h_0) = \nabla\cdot(T\nabla\bar{h}) + \bar{q}_i\delta(\boldsymbol{x}-\boldsymbol{x}_i)$$

which may be written as:

$$sS\bar{h} \pm \nabla\cdot(T\nabla\bar{h}) - \bar{f} = 0$$

where:

$$\bar{f} = \bar{q}_i\delta(\boldsymbol{x}-\boldsymbol{x}_i) + Sh_0$$

and where the Laplace transform of any given function $F(\boldsymbol{x},t)$ is indicated by an overbar, *i.e.*:

$$\mathcal{L}[F(\boldsymbol{x},t)] = \int_0^\infty F(\boldsymbol{x},t)e^{-st}dt = \bar{F}(\boldsymbol{x},s)]$$

Let:

$$\hat{h}(\boldsymbol{x},t) = \sum_{j=1}^{N} h_j(t)w_j(\boldsymbol{x})$$

be a discrete approximation of $h(\boldsymbol{x},t)$, where $h_j(t)$ is the hydraulic head at the jth node, j = 1, 2,

... , N, and where $w_j(\boldsymbol{x})$ is some spatial weighting function. Taking the Laplace transform of the matrix flow equation and substituting for $\mathcal{L}[\boldsymbol{h}]$ we obtain:

$$sS\sum_{j=1}^{N}\bar{h}_j w_j \pm \nabla\cdot\left(T\sum_{j=1}^{N}\bar{h}_j\nabla w_j\right) - \bar{f} = 0$$

or:

$$\sum_{j=1}^{N}\bar{h}_j[sSw_j \mp \nabla\cdot(T\nabla w_j)] - \bar{f} = 0$$

Requiring orthogonality with respect to the weighting functions, and choosing weighting functions that are defined piecewise on individual element areas A^e, so that $w_i = 0$ for $\boldsymbol{x}_i \notin A^e$, gives:

$$\begin{aligned}
0 &= \int_A\left\{\sum_{j=1}^{N}\bar{h}_j[sSw_j - \nabla\cdot(T\nabla w_j)] - \bar{f}\right\}w_i dA \\
&= \sum_{j=1}^{N}\bar{h}_j\sum_e\int_{A^e}[sSw_i w_j - w_i\nabla\cdot(T\nabla w_j) - \bar{f}w_i]dA \\
&= \sum_{j=1}^{N}\bar{h}_j\sum_e\left(\int_{A^e}sSw_i w_j dA - \int_{A^e}w_i\nabla T\cdot\nabla w_j dA - \int_{A^e}w_i T\nabla^2 w_j dA\right) \\
&\quad - \int_A\bar{q}_i w_i dA - \sum_{j=1}^{N}h_j(0)\sum_e\int_{A^e}Sw_i w_j dA
\end{aligned}$$

where the summation over e is understood to indicate summation over all elements e. If node locations are chosen such that any source/sink term q_i coincides with a node at $\boldsymbol{x}_i$, then

$\int_A\bar{q}_i w_i dA = \bar{q}_i$ since $w_i = 1$ at $\boldsymbol{x}_i$.

For constant $S(\boldsymbol{x}) = S_e$ and $T(\boldsymbol{x}) = T_e$ over each element, $\nabla T = 0$ giving:

$$\sum_{j=1}^{N} \bar{h}_j \sum_e \left(sS_e \int_{A^e} w_i w_j dA \pm T_e \int_{A^e} w_i \nabla^2 w_j dA \right) = \bar{q}_i + \sum_{j=1}^{N} h_j(0) \sum_e \left(S_e \int_{A^e} w_i w_j dA \right)$$

or:

$$\sum_{j=1}^{N} \bar{h}_j \sum_e (sS_e d_{ij}^e \pm T_e a_{ij}^e) = \bar{q}_i + \sum_{j=1}^{N} h_j(0) \sum_e S_e d_{ij}^e$$

where:

$$d_{ij}^e = \int_{A^e} w_i w_j dA$$

$$a_{ij}^e = \int_{A^e} w_i \nabla^2 w_j dA = \int_{A^e} \nabla \cdot (w_i \nabla w_j) dA - \int_{A^e} \nabla w_i \cdot \nabla w_j dA$$

$$= \int_{\partial A^e} w_i \nabla w_j \cdot \nabla \boldsymbol{n}\, ds - \int_{A^e} \nabla w_i \cdot \nabla w_j dA$$

by Gauss' divergence theorem. Defining the NxN matrices $\mathbf{A} = [\sum T_e a^e{}_{ij}]$ and $\mathbf{D} = [\sum S_e d^e{}_{ij}]$ and the 1xN column vectors $\boldsymbol{h}(t) = [h_j(t)]^T$ and $\boldsymbol{q}(t) = [q_i(t)]^T$, this may be written as:

$$[s\mathbf{D} \mp \mathbf{A}]\bar{\boldsymbol{h}}(s) = \bar{\boldsymbol{q}}(s) + \mathbf{D}\boldsymbol{h}(0)$$

where overbars denote Laplace transforms with respect to t.

The corresponding matrix equation for the case of steady-state flow is obtained in a similar fashion but without using the Laplace transform. Letting $\partial h/\partial t = 0$ in gives the steady-state flow equation:

$$S\frac{\partial h}{\partial t} + \nabla \cdot (T \nabla h) = q_i \delta(\boldsymbol{x} - \boldsymbol{x}_i)$$

By substituting the piecewise linear approximation for $h(\boldsymbol{x})$, and requiring orthogonality with respect to the weighting functions w_i, the matrix equation obtained is:

$$\mathbf{A}\boldsymbol{h}(t) \;=\; \boldsymbol{q}(t) \;+\; \mathbf{D}\boldsymbol{h}(0)$$

If instead of assuming constant $S(\boldsymbol{x})$and $T(\boldsymbol{x})$ over each element, these are taken to be piecewise linear:

$$T(\boldsymbol{x}) \;=\; \sum_{k=1}^{N} T_k w_k(\boldsymbol{x}) \;=\; \sum_e \sum_{k\in e} T_k w_k(\boldsymbol{x})$$

$$S(\boldsymbol{x}) \;=\; \sum_{k=1}^{N} T_k w_k(\boldsymbol{x}) \;=\; \sum_e \sum_{k\in e} T_k w_k(\boldsymbol{x})$$

then the matrices **A** and **D** are replaced by:

$$\mathbf{D} \;=\; \left[\sum_e \sum_{k\in e} S_k d^e_{ijk}\right], \qquad d^e_{ijk} \;=\; \int_{A^e} w_i w_j w_k \, dA$$

$$\mathbf{A} \;=\; \left[\sum_e \sum_{k\in e} T_k a^e_{ijk}\right], \qquad a^e_{ijk} \;=\; \int_{A^e} w_i [\nabla\cdot(w_k \nabla w_j)] \, dA$$

By expanding the dot product in the expresion for hte matrix coefficients a_{ijk} and making use of the identity $\nabla\cdot(w_i w_k \nabla w_j) = \nabla(w_i w_k)\cdot\nabla w_j + w_i w_k \nabla^2 w_j$, the coefficients a_{ijk} can be expressed as:

$$a_{ijk}(\boldsymbol{x}) \;=\; \int_{A^e} w_i (\nabla w_k \cdot \nabla w_j) \, dA \;+\; \int_{A^e} w_i w_k \nabla^2 w_j \, dA$$

$$\;=\; \int_{A^e} w_i (\nabla w_k \cdot \nabla w_j) \, dA \;+\; \int_{A^e} \nabla\cdot(w_i w_k \nabla w_j) \, dA \;-\; \int_{A^e} \nabla(w_i w_k \;+\; w_i w_k)\cdot\nabla w_j \, dA$$

$$\;=\; \int_{\partial A^e} w_i w_k \nabla w_j \cdot \boldsymbol{n} \, ds \;-\; \int_{A^e} (\nabla w_i \cdot \nabla w_j) w_k \, dA$$

Laplace-Galerkin formulation of transport problem

At a given point $\boldsymbol{x}$ in a fracture zone with effective 2-D hydrodynamic dispersion tensor $\mathbf{D}(\boldsymbol{x})$, the mass balance equation for a single non-sorbing solute species is (neglecting matrix diffusion):

$$\frac{\partial c}{\partial t} + \boldsymbol{v}\cdot\nabla c - \nabla\cdot(\mathbf{D}\nabla c) + q_c = 0$$

where $\boldsymbol{v}(\boldsymbol{x})$ is the advective velocity ($\boldsymbol{q}/\theta$), c is the concentration (averaged over the aquifer thickness), and $q_c(\boldsymbol{x})$ is the total mass influx through the two sides of the fracture zone.

For the case of a linearly and reversibly sorbing tracer, the first term in Equation 1 is modified as:

$$R\frac{\partial c}{\partial t} + \boldsymbol{v}\cdot\nabla c - \nabla\cdot(\mathbf{D}\nabla c) + q_c = 0$$

where $R = R(\boldsymbol{x})$ is a retardation coefficient accounting for surface sorption. Taking the Laplace transform with respect to t gives:

$$R(s\bar{c} - c_0) + \boldsymbol{v}\cdot\nabla\bar{c} - \nabla\cdot(\mathbf{D}\nabla\bar{c}) + \bar{q}_c = 0$$

Let:

$$\hat{c}(\boldsymbol{x},t) = \sum_{j=1}^{N} c_j(t) w_j(\boldsymbol{x})$$

be a discrete approximation of $c(\boldsymbol{x},t)$, where $c_j(t)$ is the concentration at the jth node, j = 1, 2, ... , N, and where $w_j(\boldsymbol{x})$ is some spatial weighting function.

Taking the Laplace transform and substituting for $\mathcal{L}[\boldsymbol{c}]$ in (4) we obtain:

$$R\left[s\sum_{j=1}^{N}\bar{c}_j w_j \;-\; \sum_{j=1}^{N} c_j(0) w_j\right] \;+\; \sum_{j=1}^{N}\bar{c}_j\,[\boldsymbol{v}\cdot\nabla w_j - \nabla\cdot(\mathbf{D}\nabla w_j)] \;+\; \bar{q}_c \;=\; 0$$

or:

$$\sum_{j=1}^{N}\bar{c}_j\,[Rs w_j + \boldsymbol{v}\cdot\nabla w_j - \nabla\cdot(\mathbf{D}\nabla w_j)] \;+\; \bar{q}_c \;-\; Rc_0\sum_{j=1}^{N} c_j(0) w_j \;=\; 0$$

Requiring orthogonality with respect to the weighting functions, and choosing weighting functions that are defined piecewise on individual element areas A^e, so that $w_i = 0$ for $\mathbf{x}_i \notin A^e$, gives:

$$0 \;=\; \int_A \left\{\sum_{j=1}^{N}\bar{c}_j\,[Rs w_j + \boldsymbol{v}\cdot\nabla w_j - \nabla\cdot(\mathbf{D}\nabla w_j)] \;+\; \bar{q}_c \;-\; R\sum_{j=1}^{N} c_j(0) w_j\right\} w_i\, dA$$

$$= \sum_{j=1}^{N}\bar{c}_j \sum_e \int_{A^e} [Rs w_i w_j \;+\; w_i \boldsymbol{v}\cdot\nabla w_j \;-\; w_i\nabla\cdot(\mathbf{D}\nabla w_j)]\, dA$$

$$+ \int_{A^e}\bar{q}_c w_i \;-\; \sum_{j=1}^{N} c_j(0)\sum_e \int_{A^e} R w_i w_j\, dA$$

or:

$$\sum_{j=1}^{N}\bar{c}_j \sum_e \left(s\int_{A^e} R w_i w_j\, dA \;+\; \int_{A^e} w_i \boldsymbol{v}\cdot\nabla w_j\, dA \;-\; \int_{A^e} w_i\nabla\cdot(\mathbf{D}\nabla w_j)\, dA\right)$$

$$= \;-\int_A \bar{q}_{c_i} w_i\, dA \;+\; \sum_{j=1}^{N} c_j(0)\sum_e \int_{A^e} R w_i w_j\, dA$$

where the summation over e is understood to indicate summation over all elements e , and

$$\int_A \bar{q}_{c_i} w_i dA = \bar{q}_{c_i}$$

where summation over the doubled indices *m* and *n* is implied.

If node locations are chosen such that any source/sink term q_{ci} coincides with a node at $\boldsymbol{x}_i$, then:

$$h(\boldsymbol{x}) \approx \sum_{k=1}^{N} h_k w_k(\boldsymbol{x}) \int_A \bar{q}_{c_i} w_i dA = \bar{q}_{c_i}$$

since $w_i = 1$ at $\boldsymbol{x}_i$.

Thus:

$$\sum_{j=1}^{N} \bar{c}_j \left(\sum_e s b_{ij} + \sum_e u_{ij} \right) = \sum_{j=1}^{N} c_j(0) \sum_e b_{ij} - \bar{q}_{c_i}$$

where:

$$b_{ij}^e = \int_{A^e} R w_i w_j dA$$

$$u_{ij}^e = \int_{A^e} w_i \boldsymbol{v} \cdot \nabla w_j dA - \int_{A^e} w_i \nabla \cdot (\mathbf{D} \nabla w_j) dA$$

The result can also be expressed in matrix notation as:

$$[s\mathbf{B} - \mathbf{U}]\bar{\boldsymbol{c}}(s) = \mathbf{B}\boldsymbol{c}(0) - \bar{\boldsymbol{q}}_c(s)$$

where **B** and **U** are NxN matrices $\mathbf{B} = [\sum b^e_{ij}]$ and $\mathbf{U} = [\sum u^e_{ij}]$ and $\boldsymbol{c}(t) = [c_j(t)]^T$ and $\boldsymbol{q}_c(t) = [q_{ci}(t)]^T$ are 1xN column vectors.

Under the assumption of a steady-state flow field, $\boldsymbol{v}$ is a constant vector satisfying $\boldsymbol{v} = -(T/b_T)\nabla h$, where b_T is an effective transport aperture (pore volume per unit area). Using the same piecewise-linear approximation for head as in the finite element flow model:

$$h(\boldsymbol{x}) \approx \sum_{k=1}^{N} h_k w_k(\boldsymbol{x})$$

where h_j are the nodal head coefficents determined from a steady-state flow calculation, this gives:

$$\boldsymbol{v}(\boldsymbol{x}) \approx \frac{-T(\boldsymbol{x})}{b_T(\boldsymbol{x})} \sum_{k \in e}^{N} h_k \nabla w_k(\boldsymbol{x})$$

Substituting this approximation into the previous expressions for the coefficents b_{ij} and u_{ij} gives:

$$b^e_{ij} = \int_{A^e} R w_i w_j dA$$

$$u^e_{ij} = \sum_{k \in e} h_k \int_{A^e} \frac{T}{b_T} w_i \nabla w_j \cdot \nabla w_k dA - \int_{A^e} w_i \nabla \cdot (\mathbf{D} \nabla w_j) dA$$

The above integrals depend only on the weighting functions, the calculated nodal heads, and the hydrologic properties **D**, T, and b_T, which are assumed to be constant with respect to time. Typically the principal directions of the dispersion tensor **D** will depend on the direction of the hydraulic gradient, and hence the last term in the result for u_{ij} will be related to the h_k.

Calculation of element coefficients

The principal directions of the local dispersion tensor $\mathbf{D} = [d_{ij}]$ $(i,j = 1,2)$ need to be determined from the local direction of the hydraulic gradient ∇h. Let $\boldsymbol{y}$ denote a 2-D system of Cartesian coordinates within the plane of an element, such that the coordinate y_1 is aligned with $-\nabla h$ and y_2 is in the perpendicular direction. The dispersion tensor in the $\boldsymbol{y}$ system is assumed to be:

$$\mathbf{D}_y = \begin{bmatrix} D_L + D_m & 0 \\ 0 & D_T + D_m \end{bmatrix}$$

where:

$D_L = v\alpha_L$ is the longitudinal dispersion coefficient,

$D_T = v\alpha_T$ is the longitudinal dispersion coefficient,

$v = |\boldsymbol{v}| = (T/b_T)|\nabla h|$ is the magnitude of the fluid velocity, and

D_m = coefficient of molecular diffusion.

For convenience we also define:

$D_L' = D_L + D_m$

$D_T' = D_T + D_m$

Let $\boldsymbol{x}$ denote a second 2-D system of Cartesian coordinates in the plane of the element (*e.g.*, the coordinates used to define the element geometry), with $\boldsymbol{x} = \mathbf{0}$ located at the same physical point as $\boldsymbol{y} = \mathbf{0}$. The coordinate transformation from the $\boldsymbol{y}$ system to the $\boldsymbol{x}$ system is defined in terms of a tensor with constant coefficients:

$$a_{ij} = \frac{\partial x_i}{\partial y_j}$$

so that $x_i = a_{ij} y_j$. The inverse transformation is:

$$a'_{ij} = \frac{\partial y_i}{\partial x_j} = a_{ji}$$

It is easily confirmed that the components a_{ij} are related to ∇h as:

$$\left[a_{ij}\right] = \frac{-1}{|\nabla h|}\begin{bmatrix} \frac{\partial h}{\partial x_1} & \frac{\partial h}{\partial x_2} \\ -\frac{\partial h}{\partial x_2} & \frac{\partial h}{\partial x_1} \end{bmatrix}$$

The scalar quantity $\nabla \cdot(\mathbf{D}\nabla c)$ must be invariant with respect to coordinate transformation, hence:

$$\nabla_{\boldsymbol{x}} \cdot (\mathbf{D}_{\boldsymbol{x}} \nabla_{\boldsymbol{x}} c) = \nabla_{\boldsymbol{y}} \cdot (\mathbf{D}_{\boldsymbol{y}} \nabla_{\boldsymbol{y}} c)$$

where the subscripts ***x*** and ***y*** denote which coordinate system is being referred to. In tensor notation (with the convention of summation on doubled indices) this can be written and expanded as:

$$\frac{\partial}{\partial x_i} d_{ij_x} \frac{\partial c}{\partial x_j} = \frac{\partial}{\partial y_k} d_{kl_y} \frac{\partial c}{\partial y_l}$$

$$a_{ik} \frac{\partial}{\partial y_k} d_{ij_x} a_{jl} \frac{\partial c}{\partial y_l} = \frac{\partial}{\partial y_k} d_{kl_y} \frac{\partial c}{\partial y_l}$$

$$\frac{\partial}{\partial y_k} a_{ik} d_{ij_x} a_{jl} \frac{\partial c}{\partial y_l} = \frac{\partial}{\partial y_k} d_{kl_y} \frac{\partial c}{\partial y_l}$$

yielding the relationship between the dispersion tensor components in the ***x*** and ***y*** systems:

$$d_{kl_y} = a_{ik} d_{ij_x} a_{jl}$$

Making use of the relationship between the forward and inverse transformations as given above, we obtain:

$$
\begin{aligned}
d_{kl_y} &= a'_{ki} d_{ij_x} a_{jl} \\
a_{mk} d_{kl_y} a'_{ln} &= a_{mk} a'_{ki} d_{ij_x} a_{jl} a'_{ln} \\
a_{mk} d_{kl_y} a_{nl} &= \delta_{mi} d_{ij_x} \delta_{jn} \\
a_{mk} d_{kl_y} a_{nl} &= d_{mn_x} \delta_{jn}
\end{aligned}
$$

which by replacing dummy indices yields the inverse relationship:

$$
d_{kl_x} = a_{ki} d_{ij_y} a_{lj}
$$

Expanding the second term in the previously obtained result for u_{ij} in tensor notation gives:

$$
\begin{aligned}
u^e_{ij\ II} &= \int_{A^e} w_i \nabla\cdot(\mathbf{D}\nabla w_j) dA = \int_{A^e} w_i \frac{\partial}{\partial x_m}\left(d_{mn_x} \frac{\partial w_j}{\partial x_n} \right) dA \\
&= \int_{A^e} w_i \frac{\partial d_{mn_x}}{\partial x_m} \frac{\partial w_j}{\partial x_n} dA + \int_{A^e} w_i d_{mn_x} \frac{\partial^2 w_j}{\partial x_m \partial x_n} dA
\end{aligned}
$$

For a uniform velocity field within a given element, ordinarily a uniform **D** will be assumed, so $\partial d_{mn}/\partial x_m = 0$ giving:

$$
u^e_{ij\ II} = \int_{A^e} w_i d_{mn} \frac{\partial^2 w_j}{\partial x_m \partial x_n} dA
$$

The integrand is invariant with respect to rotation of the coordinate system, since:

$$\begin{aligned} d_{mn_x}\frac{\partial^2 w_j}{\partial x_m \partial x_n}\,dA &= a_{mk}d_{kl_y}a_{nl}\frac{\partial y_p}{\partial x_m}\frac{\partial y_q}{\partial x_n}\frac{\partial^2 w_j}{\partial y_p \partial y_q} \\ &= a_{mk}d_{kl_y}a_{nl}a'_{pm}a'_{qn}\frac{\partial^2 w_j}{\partial y_p \partial y_q} \\ &= \delta_{pk}d_{kl_y}\delta_{ql}\frac{\partial^2 w_j}{\partial y_p \partial y_q} \\ &= d_{mn_y}\frac{\partial^2 w_j}{\partial y_m \partial y_n} \end{aligned}$$

In the $\boldsymbol{y}$ coordinate system, noting that $d_{11y} = D_L'$, $d_{22y} = D_T'$, and $d_{mny} = 0$ for $m \neq n$ we obtain:

$$\begin{aligned} u^e_{ij\ II} &= \int_{A^e} w_i \left(d_{11_y}\frac{\partial^2 w_j}{\partial y_1^2} + d_{22_y}\frac{\partial^2 w_j}{\partial y_2^2} \right) dA \\ &= D_T' \int_{A^e} w_i \left(r^2\frac{\partial^2 w_j}{\partial y_1^2} + \frac{\partial^2 w_j}{\partial y_2^2} \right) dA \end{aligned}$$

where $r = \sqrt{(D_L'/D_T')}$.

This integral can be evaluated more easily by mapping it to a modified coordinate system $\boldsymbol{z}$: $\{z_1 = y_1/r,\ z_2 = y_2\}$, so $r^2\partial^2 w/\partial y_1^2 = \partial^2 w/\partial z_1^2$ and $dA_y = r dA_z$, giving:

$$u_{ij\ II}^{e} = D_T' \int_{A_z^e} w_i \left(\frac{\partial^2 w_j}{\partial z_1^{\,2}} + \frac{\partial^2 w_j}{\partial z_2^{\,2}} \right) r dA_z$$

$$= r D_T' \int_{A_z^e} w_i \nabla_z^2 w_j dA_z$$

$$= \sqrt{D_L' D_T'} \int_{A_z^e} w_i \nabla_z^2 w_j dA_z$$

$$= \sqrt{D_L' D_T'} \left[\int_{\partial A_z^e} w_i \nabla_z w_j \cdot \mathbf{n}\, ds_z - \int_{A_z^e} \nabla_z w_i \cdot \nabla_z w_j dA_z \right]$$

Note that the quantity in square braces is equal to a_{ij}^{e}/T_e as defined for the finite-element model for flow.

Thus in the case of uniform T_e and b_T within each element, the coefficients u_{ij}^{e} can be calculated as:

$$u_{ij}^{e} = u_{ij\ I}^{e} - u_{ij\ II}^{e}$$

where the first term:

$$u_{ij\ I}^{e} = \frac{T}{b_T} \sum_{k \in e} h_k \int_{A^e} w_i \nabla w_j \cdot \nabla w_k dA$$

contains an integral identical to the second term in the expression for a_{ijk}^{e}, and where the second term is readily calculated as:

$$u_{ij\ II}^{e} = \frac{\sqrt{D_L' D_T'}}{T_e} a_{ij\ z}^{e}$$

Appendix C Correspondence of particle radius distribution and penetration-distance relationship

For a matrix composed of a large assemblage of spherical particles with any radius distribution $f(r) \geq 0$ on $r = [0,\infty]$, satisfying:

$$\int_0^\infty f(r)dr = 1$$

Let $V(s)$ be the volume of matrix within a skin depth s of the surface of any particle. The complementary volume of matrix which is **not** within a skin depth s of the surface:

$$\overline{V}(s) = V_{total} - V(s)$$

is related to $f(r)$ by:

$$\overline{V}(s) = \int_s^\infty f(r)\,\tfrac{4\pi}{3}(r-s)^3\,dr$$

Differentiating this with respect to the skin depth s (noting that s is in the lower limit of the integral as well as in the integrand) gives:

$$\frac{d\overline{V}}{ds} = -4\pi\int_s^\infty f(r)(r-s)^2\,dr - f(r)\frac{4\pi}{3}(r-s)^3\Big|_{r=s} = -4\pi\int_s^\infty f(r)(r-s)^2\,dr$$

Since V_{total} is constant, the first derivative of $V(s)$ is simply the negative of the preceding expression:

$$\frac{dV}{ds} = 4\pi\int_s^\infty f(r)(r-s)^2\,dr$$

Exponential case

For the case of an exponential distribution of particle radius:

$$f(r) = \lambda e^{-\lambda r}$$

the corresponding first derivative of $V(s)$ is obtained by straightforward integration:

$$\frac{dV}{ds} = 4\pi \int_s^\infty \lambda e^{-\lambda r} (r - s)^2 \, dr = 4\pi\lambda e^{-\lambda s} \int_0^\infty e^{-\lambda t} t^2 \, dt = \frac{8\pi}{\lambda^2} e^{-\lambda s}$$

making use of the substitution $t = r–s$. Thus this function has the same form as the exponential distribution, but scaled by a constant $8\pi/\lambda^3$.

Appendix D Volume-depth relationship for a regular fractal assemblage of cubes

Consider the set of cube-shaped fragments formed by the following process: Beginning with an arbitrarily large cube of side length L_0, divide the cube into 8 equal cubes of side length $L_1 = L_0/2$, and choose a fraction $a/8$ of these cubes. For $n = 1,2, ..., \infty$, take the chosen fraction of cubes from the previous step, and subdivide each into 8 equal cubes of side length $L_n = L_{n-1}/2$, and choose the same fraction $a/8$ of those.

In the assemblage of cubes resulting from this process, each cube contains a copies of itself, scaled by a factor of ½. The similarity dimension of such a set (Falconer, 1990) is thus $D = -\log a/\log(½) = \log a/\log 2$.

The number of undivided cubes of a given side length $L_n = 2^{-n}L_0$ is $N(L_n) = (8-a)a^n$. For large n the limiting log slope of the particle size distribution $N(L_n)$ versus L_n is:

$$\lim_{n\to\infty} \frac{\log N(L_n)}{\log L_n} = \lim_{n\to\infty} \frac{\log L_0 + \log(8-a) + n\log a}{\log L_0 - n\log 2} = -\frac{\log a}{\log 2} = -D$$

Thus this assemblage has a (discrete) power-law size distribution with exponent $-D$.

We note that choosing $a = 1$yields a constant (discrete) distribution of particle sizes with $D = 0$. Choosing $a = 2$ yields $D = 1$, $a = 4$ yields $D = 2$, and $a = 8$ yields $D = 3$. These values pertain to space-filling processes of dimension D.

To illustrate this, suppose that at each step of the process, we always choose to subdivide $a = 2$ cubes along a major diagonal of the original cube. This process condenses to that diagonal line (a 1-D geometry). If at each step we always choose to subdivide $a = 4$ cubes along a vertical plane that slices diagonally across the original cube, this process condenses to that plane (a 2-D geometry). If at each step we choose to subdivide all $a = 8$ cubes, we fill the entire 3-D space of the original cube with vanishingly small cubes. In the case $a = 1$, the process condenses to a single point (a zero-dimensional geometry).

Thus we may regard the similarity dimension D as representing the dimension of the process. For values of a leading to non-integral values of D, we may regard D as the "fractal" dimension of this process, following Mandelbrot (1982). From this we may note the correspondence between the negative exponent of a power-law distribution of particle sizes, and the fractal dimension of the resulting set of particles.

For the present study we are interested in the incremental volume of matrix as a function of skin depth from the surface of a particle. For a given cube of side length L_n, the volume within a skin depth s of the surface is:

$$V_n(s) = \begin{cases} L_n^3 - (L_n - 2s)^3, & s \le L_n / 2 \\ L_n^3, & s \ge L_n / 2 \end{cases}$$

and the derivative of V_n with respect to s is:

$$V_n'(s) = \frac{dV_n}{ds} = \begin{cases} 3(L_n - 2s)^2, & s \le L_n / 2 \\ 0, & s \ge L_n / 2 \end{cases}$$

The total incremental volume function $V'(s)$ is obtained by summing over all cubes:

$$V'(s) = \sum_{n=0}^{\infty} N_n V_n'(s)$$

Since cubes of side length $L_n \le 2s$ do not contribute to $V'(s)$, we may limit the summation to:

$$V'(s) = \sum_{n=0}^{m} N_n V_n'(s), \qquad m = \mathrm{int}\left(\frac{\log(L_0 / s)}{\log 2}\right) - 1$$

Substituting the previous expression for $N(L_n)$ and noting that $L_n = 2^{-n}L_0$, we obtain:

$$V'(s) = \sum_{n=0}^{m} (8-a)a^n \cdot 3\left(2^{-n} L_0 - 2s\right)$$

which simplifies to:

$$V'(s) = 6L_0(8-a)\sum_{n=0}^{m}\left(2^{-(n+1)} - \frac{s}{L_0}\right)a^n$$

with m as defined above. For comparison to data, we need only the log slope of $V'(s)$ vs. s.

Values of the log slope for different values of a, and the corresponding D, were calculated as listed in Table D-1. The arbitrary value of L_0 does not affect the results provided it is very large relative to the values of s considered; for these calculations, $L_0 = 10^{10}$ length units was used and slopes were fitted to logarithmically spaced values of s in the range 10^{-6} to 10^2 length units. For values of $1 < a < 4$ corresponding to $0 < D < 2$, the absolute value of p is close to zero; thus the incremental matrix volume with increasing skin depth is approximately constant for D in this range. For $4 < a < 8$ corresponding to $2 < D < 3$, we obtain $p \approx 2-D$ within the apparent numerical precision.

Table D-1. Numerically calculated values of p, the log slope of $V'(s)$ for the fractal cube model as a function of a and the corresponding fractal dimension D of the particle size distribution. Note the result for $a/8 = 1.000^{(*)}$ was obtained using $a = 8 - 10^{-6}$ since the above formula becomes indeterminate for this value.

$a/8$	D	p
0.1250	0.000	-2.4×10^{-8}
0.1875	0.585	-3.9×10^{-8}
0.2500	1.000	-1.8×10^{-7}
0.3125	1.322	-4.2×10^{-6}
0.3750	1.585	-1.2×10^{-4}
0.4375	1.807	-2.7×10^{-3}
0.5000	2.000	-0.040
0.5625	2.170	-0.174
0.6250	2.322	-0.322
0.6875	2.459	-0.460
0.7500	2.585	-0.585
0.8125	2.700	-0.701
0.8750	2.807	-0.808
0.9375	2.907	-0.908
0.9500	2.926	-0.927
0.9625	2.945	-0.946
0.9750	2.963	-0.964
0.9875	2.982	-0.983
0.9938	2.991	-0.992
0.9950	2.993	-0.994
0.9962	2.995	-0.995
0.9975	2.996	-0.997
0.9988	2.998	-0.999
$1.0000^{(*)}$	3.000	-1.000

www.ski.se

STATENS KÄRNKRAFTINSPEKTION
Swedish Nuclear Power Inspectorate

POST/POSTAL ADDRESS SE-106 58 Stockholm
BESÖK/OFFICE Klarabergsviadukten 90
TELEFON/TELEPHONE +46 (0)8 698 84 00
TELEFAX +46 (0)8 661 90 86
E-POST/E-MAIL ski@ski.se
WEBBPLATS/WEB SITE www.ski.se